



Electrochemical Application and AFM Characterization of Nanocomposites: Focus on Interphase Properties

HUI HUANG
黄惠

Doctoral Thesis
KTH Royal Institute of Technology
School of Chemical Science and Engineering
Division of Surface and Corrosion Science
Stockholm, Sweden, 2017

Akademisk avhandling som med tillstånd av Kungliga Tekniska Högskolan i Stockholm framlägges till offentlig granskning för avläggande av tekniska doktorsexamen fredagen den 10 March kl. 10:00 i Sal F3, Lindstedtsvägen 26, KTH, Stockholm. Avhandlingen försvaras på engelska.

Electrochemical Application and AFM Characterization of Nanocomposites: Focus on Interphase Properties

Hui Huang (huihuang@kth.se)

Doctoral Thesis

KTH Royal Institute of Technology

School of Chemical Science and Engineering

Surface and Corrosion Science

SE-100 44 Stockholm

Sweden

TRITA-CHE Report 2017:13

ISSN 1654-1081

ISBN 978-91-7729-285-2

Denna avhandling är skyddad enligt upphovsrättslagen. Alla rättigheter förbehålles.

Copyright © 2017 Hui Huang. All rights reserved. No part of this thesis may be reproduced by any means without permission from the author.

The following items are printed with permission:

PAPER I: © 2014 Elsevier.

PAPER II: © 2016 Elsevier.

PAPER III: © 2016 The Royal Society of Chemistry.

PAPER V: © 2017 Elsevier.

Printed at Universitetsservice US-AB, Stockholm 2017

To my family

***God made solids, but surfaces were the work of
the devil.***

——Wolfgang Pauli

Abstract

The use of graphene and conductive polyaniline nanomaterials in the field of electrochemistry is increasing due to their excellent conductivity, rapid electron transfer and high specific surface area. However, these properties are strongly dependent on the preparation processes. To accelerate the development of advanced electrochemical sensors for the simultaneous detection of trace amounts of heavy metal ions, two facile and green methods are proposed to improve their performance in this thesis. The first one was dedicated to make graphene-carbon nanotube hybrid nanocomposites. The introduction of carbon nanotubes not only greatly enhances the conductivity of graphene but also suppresses, to some degree, the aggregation between graphene nanosheets. Another method proposed in this thesis work was to synthesize a phytic acid doped polyaniline nanofiber based nanocomposite. The synergistic contribution from polyaniline nanofibers and phytic acid enhances the accumulation efficiency and the charge transfer rate of metal ions during the differential pulse anodic stripping voltammetry analysis. The above-mentioned nanocomposite modified electrodes were all successfully applied to real samples for the simultaneous detection of Cd^{2+} and Pb^{2+} with good recovery rates. Meanwhile, corrosion protection is another important branch in the field of electrochemistry. In this direction, an active alkyd-polyaniline composite coating with self-healing functionality was prepared. The polyaniline used in this thesis was doped with p-toluene sulfonic acid, which was employed to increase the conductivity of polyaniline, and 1 wt.% of as-prepared polyaniline nanoparticles were found to offer an effective conductive network for anticorrosion. Finally, the reasons that such low loading levels of nanomaterials can result in significantly reinforced properties in nanocomposites were studied with combined atomic force

microscopy (AFM) techniques. The results demonstrated that the interphase for a 40-nm-sized silica particle could extend to 55–70 nm in poly(ethyl methacrylate) (PEMA) and poly(isobutyl methacrylate) (PiBMA) polymer matrix, and the interphase exhibited a gradient distribution in surface nanomechanical properties.

Keywords: Electrochemical sensor; nanocomposite; graphene; carbon nanotubes; phytic acid; polyaniline; corrosion protection; silica nanoparticles; atomic force microscopy; interphase

Sammanfattning

Grafen och ledande polyanilin nanomaterial finner allt fler tillämpningar inom elektrokemiområdet på grund av dess utmärkta ledningsförmåga, snabba elektronöverföringshastighet och stora specifika yta. Emellertid påverkas dessa egenskaper väsentligt av framställningsprocessen. I min avhandling föreslås två rättframma och "gröna" metoder för att förbättra egenskaperna och därigenom påskynda utvecklingen av avancerade elektrokemiska sensorer för samtidig detektion av spårmängder av tungmetalljoner. Den första metoden bygger på att tillverka hybrid nanokompositer av grafen och kolnanorör. Kolnanorören förbättrar inte enbart grafens konduktivitet utan motverkar även i viss mån aggregering av grafen. Den andra metoden som föreslås i den här avhandlingen bygger på syntes av fytinsyra-dopade polyanilin nanofiber-baserade nanokompositer. De synergistiska bidragen från polyanilin nanofibrer och fytinsyra ökar ackumulationseffektiviteten och laddningsöverföringshastigheten för metaljoner vid pulsad anodisk stripping voltametrianalys. De ovan nämnda nanokompositmodifierade elektroder användes med framgång för samtidig detektion av Cd^{2+} och Pb^{2+} . I ett annat forskningsprojekt tillverkades en aktiv alkyd-polyanilin kompositbeläggning med självläkande egenskaper för korrosionsskyddstillämpningar. Den polyanilin som användes i det här projektet var dopad med p-toluen sulfonsyra, vilket ökar ledningsförmågan hos polyanilin. Endast 1 wt.% av de tillverkade polyanilin nanopartiklarna behövdes för att uppnå ett effektivt ledande nätverk med korrosionsskyddande egenskaper. Anledningen till att en så pass liten mängd nanopartiklar kan ge väsentlig förstärkning av nanokompositer undersöktes med atomkraftmikroskopimetoder (AFM). Resultaten visar att interfasen runt en 40 nm stor kiseldioxid partikel kan ha en utsträckning av 55–70 nm i en matris bestående av poly(etyl

metakrylat) (PEMA) och poly(isobutyl meakrylat) (PiBMA), och interfases nanomekaniska egenskaper beror på avståndet från partikeln.

Nyckelord: Elektrokemisk sensor, nanokomposit, grafen, kol nanorör, fytinsyra, polyanilin, korrosionsskydd, kiseldioxid nanopartikel, atomkraftmikroskop, interfase

List of papers

This doctoral thesis is a summary of key results reported in the following peer-reviewed scientific papers:

Paper I: Ultrasensitive and simultaneous detection of heavy metal ions based on three-dimensional graphene-carbon nanotubes hybrid electrode materials

Huang, H.; Chen, T.; Liu, X.; Ma, H.

Analytica Chimica Acta **2014**, 852, 45-54.

Paper II: Synthesis of a novel electrode material containing phytic acid-polyaniline nanofibers for simultaneous determination of cadmium and lead ions

Huang, H.; Zhu, W.; Gao, X.; Liu, X.; Ma, H.

Analytica Chimica Acta **2016**, 947, 32-41.

Paper III: Towards the mechanism of electrochemical activity and self-healing of 1 wt% PTSA doped polyaniline in alkyd composite polymer coating: combined AFM-based studies

Li, J.; Huang, H.; Fielden, M.; Pan, J.; Ecco, L.; Schellbach, C.; Delmas, G.; Claesson, P. M.

RSC Advances **2016**, 6, 19111-19127.

Paper IV: Local surface mechanical properties of PDMS-silica composite layers probed by Intermodulation AFM

Huang, H.; Dobryden, I.; Ejenstam, L.; Pan, J.; Fielden, M.L.; Haviland, D.; Claesson, P.M.

Submitted

Paper V: Nanomechanical characterization of PiBMA nano-composite with hydrophobic nanoparticles using AFM force

methods: The effect of temperature on particle-polymer interphase

Huang, H.; Dobryden, I.; Ihrner, N.; Johansson, M.; Ma, H.; Pan J.; Claesson, P.M.

Journal of Colloid and Interface Science **2017**, 494, 204-214.

The author's contributions to the papers included in this thesis are summarized below:

Paper I: All experimental work, data analysis and interpretation, and manuscript preparation.

Paper II: All experimental work, data analysis and interpretation, and manuscript preparation.

Paper III: Active participation and discussion in AFM measurement and data analysis of electrochemical measurements.

Paper IV: Major experimental work, data analysis and interpretation, and manuscript preparation.

Paper V: Major experimental work, data analysis and interpretation, and manuscript preparation.

Other papers not included in this thesis:

Paper I: Effects of surface morphology of nanostructured PbO₂ thin films on their electrochemical properties

Chen, T.; Huang, H.; Ma, H.; Kong, D.

Electrochimica Acta **2013**, *88*, 79-85.

Paper II: Electrochemical behavior and voltammetric determination of acetaminophen based on glassy carbon electrodes modified with poly(4-aminobenzoic acid)/electrochemically reduced graphene oxide composite films

Zhu, W.; Huang, H.; Gao, X.; Ma, H.

Materials Science and Engineering C **2014**, *45*, 21-28.

Paper III: Nickel-vanadium monolayer double hydroxide for efficient electrochemical water oxidation

Fan, K.; Chen, H.; Ji, Y.; Huang, H.; Claesson, P. M.; Daniel, Q.; Philippe, B.; Rensmo, H.; Li, F.; Luo, Y.

Nature Communications **2016**, *7*, 11981.

Summary of papers

In **Paper I** a green and facile method was developed for preparation of a new type of hybrid nanocomposite material, which was composed of one-dimensional multi-walled carbon nanotubes (MWCNTs) and two-dimensional graphene oxide (GO) sheets. After electrochemical reduction, the as-prepared graphene-MWCNTs nanomaterials were demonstrated to be a practical sensor material for the detection of heavy metal ions using differential pulse anodic stripping voltammetry (DPASV), showing excellent sensitivity and simultaneous detection performance. The linear calibration plots for Pb^{2+} and Cd^{2+} were in the range of $0.5\text{--}30\ \mu\text{g L}^{-1}$. The detection limits were determined to be $0.2\ \mu\text{g L}^{-1}$ (signal to noise, $S/N = 3$) for Pb^{2+} and $0.1\ \mu\text{g L}^{-1}$ ($S/N = 3$) for Cd^{2+} in the case of a deposition time of 180 s. This method was also successfully applied to the detection of Cd^{2+} and Pb^{2+} in real electroplating effluent samples containing significant amounts of surface-active impurities.

In **Paper II** an environmentally friendly material, phytic acid, was incorporated into polyaniline (PANI) nanofibers using the “doping-dedoping-redoping” method. The as-prepared one-dimensional nanocomposite showed better conductivity and more facile electron transfer rate than the traditionally used bulk PANI or inorganic acid doped PANI nanomaterials. The nanocomposite was evaluated as a new electrode material for simultaneous detection of trace amounts of Cd^{2+} and Pb^{2+} using DPASV. The synergistic contribution from one-dimensional PANI nanofibers and phytic acid enhances the accumulation efficiency and the charge transfer rate of metal ions during the DPASV analysis. Good linear relationships were obtained for Cd^{2+} in the range of $0.05\text{--}60\ \text{mg L}^{-1}$, with the detection limit ($S/N = 3$) of $0.02\ \text{mg L}^{-1}$, and for Pb^{2+} in the range of $0.1\text{--}60\ \text{mg L}^{-1}$, with the detection limit ($S/N = 3$) of $0.05\ \text{mg L}^{-1}$. The proposed method was also applied to real samples.

For corrosion protection with self-healing properties, an active alkyd-polyaniline composite coating was described in **Paper III**. The PANI used here was doped with p-toluene sulfonic acid, and it was employed to increase the conductivity of PANI. Just 1 wt.% of as-prepared PANI nanoparticles were found to offer an effective conductive network for anticorrosion. This study focused on a fundamental understanding of the anticorrosion mechanism of the “smart” coating for carbon steel. Combined electrochemical and AFM measurements demonstrated that the improved stability and corrosion protection by such a low loading level of PANI in the polymer matrix were due to the redox property, which leads to steel passivation.

In **Paper IV** intermodulation atomic force microscopy (ImAFM) was employed to directly measure the local mechanical properties of a PDMS-silica nanocomposite. The data analysis was carried out without inferring any contact mechanics model. Analysis of energy dissipation with ImAFM showed a lowering of the viscous response due to the presence of the hydrophobic silica nanoparticles in the PDMS matrix. The enhanced elastic response was also evident from the in-phase stiffness of the matrix, which was found increased by a factor of 1.5 in presence of the nanoparticles. Furthermore, analysis of dissipation energy and stiffness in the immediate vicinity of the nanoparticles provided an estimate of the interphase thickness. Because the local stiffness varied significantly near the nanoparticle, AFM height images contained artifacts that must be corrected in order to reveal the true surface topography. Without such a correction, the AFM height images erroneously show that the stiff particles protrude from the surface, whereas corrected images show that they are actually embedded in the matrix and likely covered with a thin layer of polymer.

In **Paper V** two AFM force methods, i.e., quantitative imaging and force mapping spectroscopy, were used to directly measure the

nanomechanical properties of the interphase in a poly(ethyl methacrylate)-poly(isobutyl methacrylate) (PEMA-PiBMA) polymer nanocomposite with high concentration of hydrophobized silica nanoparticles over a controlled temperature range. The results indicated that the interphase for a 40-nm-sized particle could extend to 55–70 nm, and the interphase region exhibited a gradient distribution in mechanical properties. The analysis of the local glass transition temperature (T_g) of the interphase and polymer matrix provides evidence for reduced stiffness of the polymer matrix in presence of high nanoparticle concentrations.

Table of Contents

Chapter 1 Introduction	1
1.1 Electrochemical sensor	1
1.1.1 Principles	1
1.1.2 Configurations.....	2
1.1.3 Analytical technique: differential pulse anodic stripping voltammetry	3
1.2 Electrode materials.....	5
1.2.1 Carbon nanomaterials: carbon nanotubes and graphene.....	5
1.2.2 Conducting polymers: polyaniline	7
1.2.3 Silica nanoparticles.....	10
1.3 Electrochemical applications of nanocomposites.....	11
1.3.1 Detection of heavy metal ions.....	11
1.3.2 Corrosion protection by PANI-alkyd nanocomposite	11
1.4 Why nanomaterials?	12
1.4.1 Interphase and interface in polymeric composites.....	13
1.4.2 Characterization of the interphase by AFM	13
Chapter 2 Materials and methods	15
2.1 Synthesis of GO-MWCNTs nanocomposite	15
2.2 Fabrication of graphene-MWCNTs modified working electrodes.....	16
2.3 Synthesis of the phytic acid-polyaniline nanocomposite	16
2.4 Fabrication of the phytic acid-polyaniline nanocomposite modified electrodes	17
2.5 Synthesis of the PDMS-silica nanocomposite	18
2.6 Synthesis of PEMA-PiBMA nanocomposite with hydrophobized silica nanoparticles.....	20
Chapter 3 Techniques	25
3.1 TEM and SEM.....	25
3.2 EDS analysis.....	25
3.3 Raman spectroscopy	26
3.4 FT-IR spectroscopy	26

3.5 Open-circuit potential, OCP	26
3.6 Atomic force microscopy, AFM	27
3.6.1 Tapping mode	27
3.6.2 Intermodulation AFM.....	28
3.6.3 Force mapping and QI AFM	30
Chapter 4 Key results and discussions	33
4.1 Electrochemical application of synthesized graphene-MWCNTs nanocomposites.....	33
4.1.1 Morphology, molecular and electronic structures	33
4.1.2 Electrochemical properties	35
4.1.3 Electrochemical response to heavy metal ions.....	37
4.2 Electrochemical application of synthesized phytic acid-PANI nanocomposite.....	39
4.2.1 Morphology and molecular structure.....	39
4.2.2 Electrochemical properties	42
4.2.3 Electrochemical response to heavy metal ions.....	43
4.3 Electrochemical application of the PANI-alkyd nanocomposite	46
4.3.1 Morphology.....	46
4.3.2 Electrochemical evaluation of long-term anticorrosion performance	46
4.4 AFM characterization of nanocomposites.....	48
4.4.1 Morphology characterization of PDMS/hydrophobic silica nanocomposites: Tapping mode AFM.....	48
4.4.2 Nanomechanical characterization of PDMS/hydrophobic silica nanocomposites	50
4.4.2.1 Intermodulation AFM.....	50
4.4.2.2 QI AFM and force mapping on PEMA-PiBMA/hydrophobic silica nanocomposites.....	51
4.4.3 Nanomechanical properties of the interphase found in the PEMA-PiBMA/hydrophobized silica nanocomposite	54
Chapter 5 Conclusions and impact.....	57
Chapter 6 Future work.....	59
Acknowledgments.....	61
References.....	63

Chapter 1 Introduction

Sensors are widely used in our everyday life, for example, a mercury-based glass thermometer or an oxygen sensor in a car detecting the gasoline/oxygen ratio. In electronics, a sensor is a device that detects some type of input in the physical environment and provides a corresponding output. Commonly measured inputs are temperature, moisture, pressure, light, motion, flow, heat, sound, and so on. Various outputs could be provided by the sensors, typically they constitute an electrical signal due to its easy reception, transmission and processing. Therefore, most modern sensors convert non-electrical parameters into signals that can be detected electrically.

Sensors can be classified in many different ways, for example, i) according to their applications (such as biosensors, image, humidity, or viscosity sensors), ii) based on the materials used (for instance, zirconium oxide, magnetic iron oxide, graphene, fiberoptic, ceria nanoparticle, conducting polymer sensors), iii) according to physical and chemical transduction principles (mechanical, electrical, magnetic, thermo-optical effects etc.) or by other possible classification criteria.¹ Electrochemical sensors, which are the fundament for one of the most important instrumental analysis methods, are based on the electrochemical transduction principle. This technology, which is specially considered in this thesis, provides sensitive, inexpensive, portable and selective devices.

1.1 Electrochemical sensor

1.1.1 Principles

In the broadest definition, electrochemistry is the subject that studies and explores the mutual conversion between electrical

energy and chemical energy. This conversion involves transfer of electric charges between electrodes and electrolytes, that is, redox reactions take place at interfaces (such as gas/liquid, liquid/solid, liquid/liquid interfaces). Electrochemical sensors are devices or instruments that determine the concentration or composition of specific chemical substances by measuring changes in potential, current or resistance due to the presence of the analytes. Electrochemical sensors have many favorable properties. They consume very little power to operate and are easy to miniaturize.² Therefore, they are extensively used in many stationary and portable devices for the determination of electroactive substances. In this thesis work, for example, toxic heavy metal ions in aqueous solution were monitored using an electrochemical method.

1.1.2 Configurations

There are different ways to configure electrochemical sensors, depending on the final intended usage. Typically, an electrochemical sensor is a three-electrode system and consists of a working electrode, a reference electrode and a counter electrode separated by the supporting electrolyte. The reference electrode is introduced to measure the electrode potentials for the electrochemical reactions, and it should display a highly stable electrode potential. Generally employed reference electrodes are, for instance, the standard hydrogen electrode (SHE), the saturated calomel electrode (SCE) and the silver chloride electrode (Ag/AgCl). In this thesis, a KCl-saturated SCE was used as the reference electrode, and all potentials were measured relative to this electrode. The counter electrode is also called the auxiliary electrode. It is connected with the working electrode in series to form the current circuit, and usually made of an electrochemically inert and low-resistance material that does not exhibit any polarization properties over the

applied electrochemical window. Commonly used materials for the auxiliary electrode include platinum, gold and carbon. A platinum plate was used as the counter electrode in this thesis work.

The working electrode plays a pivotal role since it is here the electron-transfer reactions that are expected in the analysis occur. Therefore, working electrodes should also show ideal polarization character over the applied potential window. Traditional materials based working electrodes include: i) mercury and inert metal (platinum and gold etc.) electrodes, ii) some metal oxides such as indium tin oxide electrode, and iii) the allotropic forms of carbon electrodes, e.g., graphite, carbon paste, carbon fiber or glassy carbon electrodes (GCE). However, the above-mentioned electrodes have not been able to meet the ever-increasing requirements for the analysis of complex samples.

Recently, solid electrodes modified with nanostructured materials have been proposed to accelerate the development of advanced sensors.³ Various excellent properties have been achieved by these sensor systems due to the favorable properties of the nanomaterials used. A comprehensive review of the contemporary nanomaterials goes beyond the purpose of this thesis. However, several useful nanomaterials are described in section 1.2.

1.1.3 Analytical technique: differential pulse anodic stripping voltammetry

For an integrated electrochemical sensor system, except for the three-electrode elements, the signal processing technique employed is also important since the detection sensitivity and selectivity are closely affected by the processing technique used. Common electrochemical methods include, for instance, cyclic voltammetry (CV), pulse voltammetry, chronoamperometry, chronocoulometry, chronopotentiometry and electrogravimetry. Among these

techniques, pulse voltammetry is often preferred due to its high sensitivity when the background current of the electrode is large or the modified electrode film is very thin. Based on the way the voltage from the outside is imposed, pulse voltammetry can be classified into normal pulse voltammetry (NPV) and differential pulse voltammetry (DPV). The difference is that a series of ever-increasing voltage pulses are superimposed on a constant initial potential in the former, while in DPV a series of voltage pulses with constant amplitude (2~100 mV) are superimposed on a linear sweep potential. The current values are sampled when the potential is changed and the current difference is plotted as a function of potential. Currently, DPV is one of the most sensitive techniques of all voltammetric methods, and the detection limit can be as low as about 10^{-8} mol L⁻¹.

To further increase the detection sensitivity, anodic stripping voltammetry (ASV) is introduced for quantitative analysis of some specific chemicals in aqueous solution such as heavy metal ions. In this thesis work, differential pulse anodic stripping voltammetry (DPASV) was used. Before the current vs. potential plot is sampled, i.e., before the stripping step, there is a preconcentration step in DPASV. Specifically, the species of interest is first deposited on the working electrode by simple adsorption or electrochemical enrichment before being stripped from the electrode. In the stripping step, the heavy metals are oxidized and the working electrode performs as an anode, explaining the name anodic stripping voltammetry. By combination of the two electrochemical steps, DPASV permits to reach an excellent detection limit as low as 10^{-10} mol L⁻¹.

In anodic stripping voltammetric analysis, the working electrode performs a pivotal role since it undertakes the responsibility not only for the effective preconcentration of metal ions in a suitable potential region but also for the adequate stripping ability. The

previously employed mercury based electrodes provide high detection sensitivity owing to liquid mercury's ability to form alloys with many metals, but mercury now become restricted due to health considerations.^{4,5} Alternatively, environmentally friendly electrodes like gold,⁶ bismuth,⁷ or stannum film⁸ etc., and chemically modified electrodes have shown great potential in substituting the mercury electrodes.^{9,10} A variety of advanced materials has been employed to modify the electrodes including carbon nanotubes,¹¹ graphene,¹² organic polymers,^{13,14} and corresponding nanocomposites.^{15,16} The fundamental principle in designing these detection platforms is to i) enrich the electrostatic adsorption active sites by introducing specific binding groups, and ii) accelerate the electron transfer rate at the electrode surface by enhancing the conductivity of the modified materials, thus increasing the overall preconcentration efficiency.

1.2 Electrode materials

1.2.1 Carbon nanomaterials: carbon nanotubes and graphene

Carbon nanotubes (CNTs) and graphene are two allotropic forms of carbon, where carbon atoms are in the sp^2 -hybridization state.¹¹ CNTs are one-dimensional nanomaterials with nanoscale diameters, but the lengths could range from a few nanometers to several centimeters. CNTs are produced in large batch by, for instance, floating catalyst chemical vapor deposition or laser evaporation.^{17,18} The as-prepared CNTs have excellent electrical conductivity, mechanical and photophysical properties. However, the primary drawback of CNTs is that there are only a few functional groups (such as $-COOH$, $-C=O$ and $-OH$) on their surfaces, making CNTs highly hydrophobic. For this reason, although with a high conductivity, unmodified CNTs are unable to chelate metal ions in

aqueous phase and do not work as good electrode materials for ASV electroanalytical purposes.

It is generally believed that graphene, a one-atom-thick layer of graphite, possesses excellent conductivity, high electron transfer rate and very large specific surface area. However, these properties are strongly dependent on the preparation process of graphene sheets. In fact, the material obtained by the reduction of graphene oxide (rGO) sheets by the well-known Hummers method,¹⁹ has much lower electrical conductivity and specific surface area than theoretically expected.²⁰ This is owing to excessive defects originating from the chemical oxidation process and the clustering caused by significant π - π interaction. Instead, the main advantage of the as-prepared rGO is its strong hydrophilicity originating from some preserved surface functional groups, which enables metal ions to strongly adsorb to rGO.

Seeing that rGO and CNTs have their own advantages and disadvantages, we utilized two-dimensional graphene oxide (GO) nanosheets and single-dimensional multi-walled carbon nanotubes (MWCNTs) to fabricate a type of graphene-MWCNTs (G-MWCNTs) hybrid nanocomposites with excellent conductivity and good water solubility. In this way, the effective combination of two carbon nanostructures can not only make full use of the respective advantages, but also counteract the deficiencies of the two building blocks. In this thesis work, a simple and green method was developed to fabricate three-dimensional G-MWCNTs nanocomposites. Thus, hydrophilic GO components interact with CNTs through π - π interaction, increasing the dispersibility of CNTs in water. At the same time, the presence of the CNTs components not only greatly enhances the conductivity of the nanocomposites but also to some degree suppresses the aggregation of GO nanosheets. Moreover, the hydrophilic hybrid nanocomposites are able to adsorb heavy metal ions from aqueous solution due to their

unusual structure and high amount of chelating groups, which make them ideal sensing nanomaterials suitable for electrochemical detection and preconcentration of trace amounts of heavy metal ions.

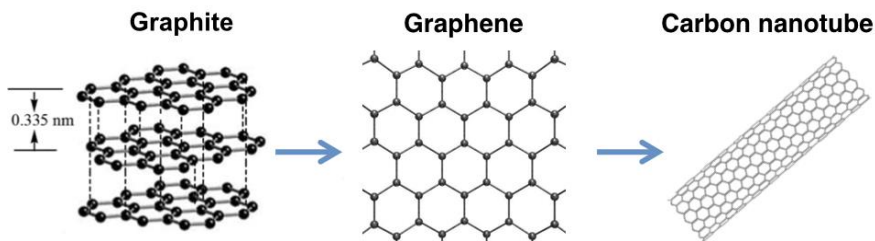


Figure 1.1. From graphite to graphene to carbon nanotube.

1.2.2 Conducting polymers: polyaniline

Before Heeger, MacDiarmid and Shirakawa reported that the conductivity of polyacetylene significantly increases upon doping with oxidized iodine in 1977, organic polymers had been regarded as insulators.²¹ In year 2000, the discovery of conductive polymers was awarded the Nobel Prize. Since then, significant efforts have been made to develop new conducting polymers and to identify new properties and applications of those materials. Nowadays, conducting polymers are found in a variety of applications and devices, such as organic light-emitting diodes (OLED), antistatic shielding, electrochromism, organic solar cells, supercapacitors, corrosion protection and electrochemical sensors. Typical conducting polymers are shown in Figure 1.2.

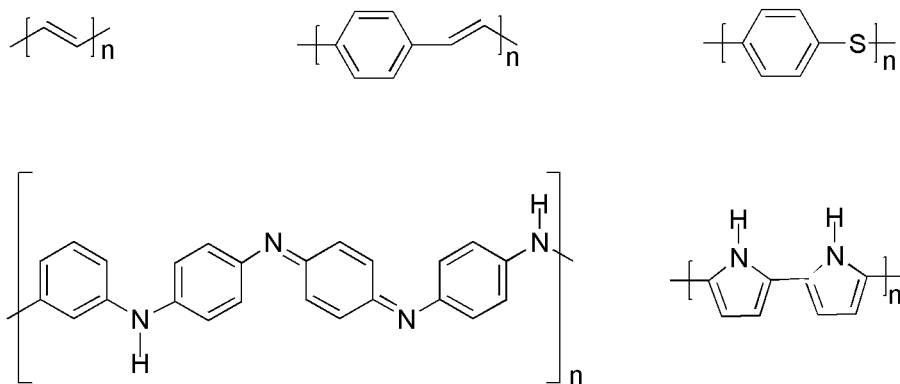


Figure 1.2. Examples of conducting polymers: polyacetylene; polyphenylene vinylene; polyphenyl sulfide; polyaniline; polypyrrole.

Polyaniline (PANI) is one of the most promising conducting polymers and many studies have been focused on PANI due to its inexpensiveness, easy synthesis, environmental stability, and reversible redox properties.^{22,23} As an electrochemical sensor material, PANI provides abundant electron active sites for binding e.g. toxic chemicals, rapid electron transfer, and tunable conductivity by simple acid-base reactions with different dopants or by incorporating other electro-conductive materials, such as carbon nanotubes, graphene and metal nanoparticles.^{15,16,23,24} Recently, versatile strategies have been explored to modify PANI for increasing the detection sensitivity towards heavy metal ions. For example, Philips et al. reported a cyano group containing PANI derivative for simultaneous detection of Pb^{2+} and Cd^{2+} using DPASV, and low detection limits, $0.255 \mu g L^{-1}$ for Cd^{2+} and $0.165 \mu g L^{-1}$ for Pb^{2+} , were obtained.¹³ Su et al. employed a thiolated PANI-multi-walled CNTs nanocomposite for DPASV determination of Pb^{2+} and Cd^{2+} , with ultra-low detection limits of 0.04 and $0.01 \mu g L^{-1}$, respectively.²⁵ In another recent study reported by Terbouche et al., humic acid-PANI composite modified cavity microelectrodes were used for detecting Ni^{2+} and Cd^{2+} via square wave voltammetry, and the limit of detection was $1.35 \mu g L^{-1}$ for Cd^{2+} .²⁶ More recently,

Ruecha et al. developed a graphene-PANI nanocomposite electrode for simultaneous detection of Zn^{2+} , Cd^{2+} and Pb^{2+} , with limits of detection of $0.1 \mu\text{g L}^{-1}$ for both Cd^{2+} and Pb^{2+} with a linear response range of $1\text{--}300 \mu\text{g L}^{-1}$.¹⁵ The progresses made in such sensors are due to two factors. First, the increased binding strength of the chelating groups compared to pure PANI, i.e., the cyano or thiol groups, or the large number of carboxyl and hydroxyl groups present in humic acid and rGO. Second, the increased conductivity achieved by using CNTs or graphene. However, the cyano and thiol dopants employed cannot be considered as being environmentally benign.

In this thesis work, phytic acid was incorporated in PANI nanofiber nanocomposites, and a glassy carbon electrode modified by the resulting nanocomposite was adopted for simultaneous detection of Cd^{2+} and Pb^{2+} using DPASV. Phytic acid, also known as inositol hexaphosphate, is a multivalent organic acid with six phosphoric acid groups ($-\text{PO}_3\text{H}_2$), each attached to one carbon of a cyclohexane (Figure 1.3). The ionizable $-\text{PO}_3\text{H}_2$ group can form complexes with heavy metal ions.²⁷ It has been reported that phytic acid and its salts can be used to remove pollutants such as Cu^{2+} , Zn^{2+} and Cd^{2+} .²⁸ In addition, phytic acid is a “green” material mainly extracted from plants, and it possesses various important properties, including nontoxicity, high chelating ability, and low cost.²⁹ However, phytic acid based materials have seldom been reported for detecting heavy metal ions, since phytic acid is very soluble in water and cannot form stable and repeatable films on the commonly used electrodes, e.g., glassy carbon and gold electrodes. To overcome this limitation, PANI was employed as an immobilization matrix for phytic acid in this thesis work.

The nanostructured PANI offers higher specific surface area, better conductivity, and more active sites for adsorbing metal ions than its traditional bulk counterpart. The $-\text{PO}_3\text{H}_2$ groups in phytic

acid are expected to further enhance the accumulation efficiency of heavy metal ions. In general, the synergistic contribution from PANI nanofibers and phytic acid makes the new material a capable candidate for the determination of trace amounts of heavy metal ions.

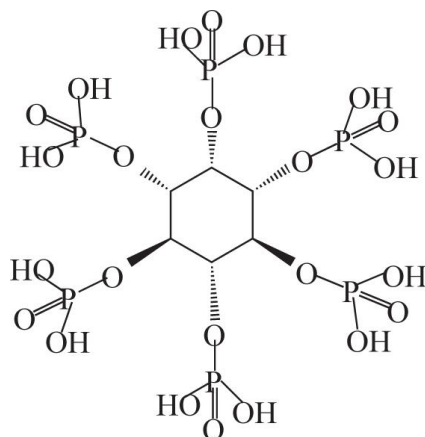


Figure 1.3. The molecular structure of phytic acid.

1.2.3 Silica nanoparticles

Silica nanoparticles have a variety of applications in chemical sensors due to its porous structure and high specific surface area. In those applications, mono-dispersed and well-defined silica particles, usually prepared by sol-gel methods, are used as carriers for immobilizing other nanomaterials, e.g., magnetic nanoparticles and quantum dots. Another crucial application for silica particles is their use as reinforcing fillers. Such particles can be obtained commercially, and they are commonly made by flame pyrolysis of silicon tetrachloride. Under normal conditions, silica nanoparticles demonstrate good chemical stability and resistance to mechanical stress. The use of silica as reinforcing fillers allows improvement of the mechanical properties of a soft polymer matrix and improvement of corrosion protection.³⁰

1.3 Electrochemical applications of nanocomposites

1.3.1 Detection of heavy metal ions

Heavy metals are natural constituents of the earth and have been widely used in industry for a few decades.³¹ However, the environmental pollution caused by the indiscriminating handling of heavy metals has received global attention in recent years.^{32,33} Among them, Cd^{2+} and Pb^{2+} are two highly toxic and persistent pollutants even at very low concentrations. They display bioaccumulation and are hard to remove from human body.^{4,34,35} Therefore, to assess and control the unwanted daily dietary intake of heavy metal ions, it is critically important to develop novel analytical materials and devices for sensitive, rapid and real-time detection of trace levels of heavy metal ions.

Various sensitive methods, for instance, atomic absorption spectroscopy, plasma atomic emission spectroscopy, spectrophotometry, X-ray and nuclear magnetic resonance, have been used for the detection of Cd^{2+} and Pb^{2+} , but they usually require expensive equipment and complicated sample preparations.^{36,37} By comparison, electrochemical nanomaterial-modified sensors have intrinsic advantages of simple operation, low cost, less sample consumption, high sensitivity, portable instrumentation and simultaneous determination capability.

1.3.2 Corrosion protection by PANI-alkyd nanocomposite

Corrosion of metals is a natural process that arises from the chemical and/or electrochemical reactions of metals. To control and retard corrosion in order to prolong material lifetimes and even avoid disasters is crucially important. Organic coatings are widely used for protection of metals by simply providing a physical

separation of the metal from ambient environment. However, due to the presence of pores and defects in the coatings, penetration of water or different kinds of ions can occur, leading to the corrosive agents eventually reaching the interface between metal and polymer. Also, defects due to aging or scratches generated by external forces are inevitable. To have long-term durability and reliability, the idea of 'self-healing' by incorporating electro-active components into the polymer matrix that counteracts the corrosion reactions has been proposed.³⁸ Recently, conducting polymers such as PANI have been successfully used as such electro-active additives to ameliorate the protection performances.³⁹ It has been reported that PANI could create a passivating oxidized thin layer at the interface between metal and polymer to protect the metal from further corrosion attack.

In this thesis work, a composite alkyd coating with 1 wt.% p-toluene sulfonic acid (PTSA) doped PANI was prepared. Improved corrosion protection and strong self-healing ability were obtained both in air and in 3 wt.% NaCl solution by such a low concentration of PANI.

1.4 Why nanomaterials?

Polymeric nanocomposites containing, e.g., carbon nanotubes,⁴⁰ graphene,⁴¹ carbon black⁴² and silica nanoparticles^{43,44} as fillers often display dramatically improved mechanical properties compared to the conventional microcomposites or the pure polymer matrix, even at low loading content. Experiments and numerical modeling have concluded that this "*nano effect*" at constant additive volume is due to the dramatic increase in the total interfacial area as the size of the additive decreases.^{45,46}

1.4.1 Interphase and interface in polymeric composites

The interfacial region, also called the interphase, is a transitional volume between filler and bulk matrix, which differs in its chemical and physical properties compared to the bulk matrix due to polymer-filler interactions. The properties of the interphase are crucial in nanocomposites not only due to its different physicochemical properties compared to the bulk matrix. This region is also responsible for the loads transfer from the matrix to the particles. The thickness of the interphase is very small, from a few nm to less than 1 μm .

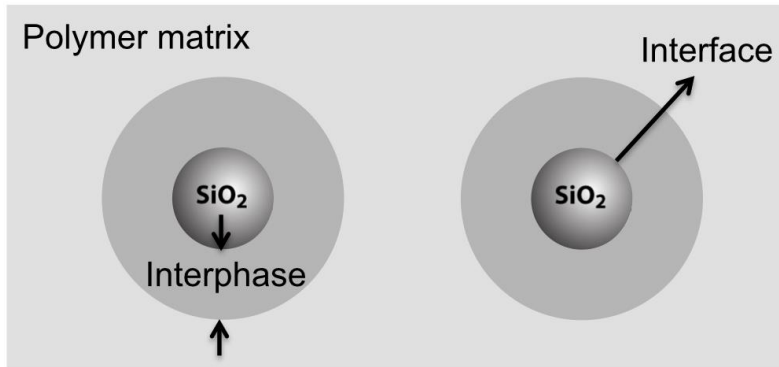


Figure 1.4. The interface is a surface formed by a common boundary between particle and the polymer matrix. The interphase is a finite region from the interface to the polymer matrix where the material properties are different from those of the polymer matrix.

1.4.2 Characterization of the interphase by AFM

Understanding the properties of the interphase is crucial in designing the desired properties of the nanocomposites.⁴⁷⁻⁴⁹ Several techniques such as the rubber process analyzer and nuclear magnetic resonance, as well as theoretical calculations, have demonstrated the existence of the matrix-filler interphase.^{42,46,50} However, it is still a challenge to directly measure the mechanical

response of the interphase around an individual nano-sized particle due to its small dimension. With the above-mentioned methods, it is impossible to distinguish nanomechanical differences between the polymer matrix and the interphase and to directly measure the elastic and viscous response of the interphase.⁵¹ Thus, detailed characterization of the properties of the interphase between individual nanoparticles and the polymer matrix is a nontrivial task. In my thesis work I addressed this issue by employing three different AFM operational modes.

It is now a generally accepted concept that nanocomposites with low loading levels of inorganic nanoparticles in a polymer matrix can have significantly different properties compared with the corresponding polymer without nanoparticles, or with micro-sized particles of the same composition.⁵²⁻⁵⁴ Numerical modeling methods combined with experimental studies have shown that this “*nano effect*” is due to the strong increase in the total volume of the interphase as the size of the filler is decreased at a constant total volume fraction of particles.^{45,55,56} The properties and structure of the interphase, especially the dimension of this region around the nanoparticles, are crucial in determining the global mechanical properties of the nanocomposite, since the interphase can become the dominating volume when the particles are nanometer-sized.⁵⁷ For example, for a given 1 vol% of spherical particles, a 1 nm thick interphase around 1 nm diameter particles shares 26% of the total volume of polymer, whereas it only takes up 0.06% of the total volume of polymer when the particles are 100 nm in diameter. This is a consequence of the huge specific surface area of a uniform dispersion of nanoparticles.

Chapter 2 Materials and methods

2.1 Synthesis of GO-MWCNTs nanocomposite

MWCNTs (purity: >95 wt.%; outer diameter: 20–30 nm; length: 0.5–2 μm , from Chengdu Organic Chemicals Co. Ltd.) were treated with mixed acids (concentrated HNO_3 : H_2SO_4 , 1:3) prior to use for about 4 h, followed by filtering, rinsing and drying. A MWCNTs dispersion (1.0 mg mL^{-1}) was obtained by ultra-sonication (1 h) of acidified MWCNTs. Further, a GO nanosheets dispersion (1.0 mg mL^{-1}) was obtained by ultra-sonication (1 h) of graphite oxides, which were synthesized from natural graphite (325 mesh, Alfa Aesar) according to a modified Hummer's method.⁵⁸ The as-prepared GO dispersion is homogeneous and brown in color (Figure 2.1). Then, the MWCNTs (10 mL) and GO (10 mL) dispersions were mixed, and the mixture was further treated by ultra-sonication (2 h). Next, excessive MWCNTs were removed by centrifugation at 5000 rpm and the unreacted GO was separated at 12500 rpm. Finally, the obtained sediment, i.e., the GO-MWCNTs nanocomposite, was collected and dried at 50 $^{\circ}\text{C}$ in a vacuum oven. This nanocomposite can form stable dispersions in water without sediment for several months.

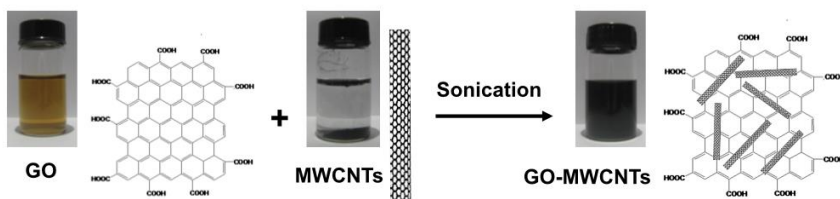


Figure 2.1. Schematic diagram illustrating the synthesis of GO-MWCNT hybrid nanomaterials.

2.2 Fabrication of graphene-MWCNTs modified working electrodes

The GO-MWCNTs dispersion (0.5 mg mL^{-1}) was obtained by ultrasonic treatment (1 h) of as-prepared GO-MWCNTs nanocomposite. Nafion, a sulfonated tetrafluoroethylene based fluoropolymer-copolymer (5 wt.% in lower aliphatic alcohols, Sigma-Aldrich), was diluted to 1 wt.% by ethanol. Prior to use, a GCE was polished carefully with $1.0 \text{ }\mu\text{m}$, $0.3 \text{ }\mu\text{m}$ and $0.05 \text{ }\mu\text{m}$ alumina slurry respectively, and washed ultrasonically with water, ethanol and ultrapure water in sequence. Then, the GCE was scanned between 0 and 2.0 V in $0.5 \text{ mol L}^{-1} \text{ H}_2\text{SO}_4$ at 100 mV s^{-1} for 50 cycles to remove possible contaminants. Next, the GO-MWCNTs dispersion ($5 \text{ }\mu\text{L}$) was cast on the electrode surface, and dried under an infrared lamp. Finally, Nafion solution ($5 \text{ }\mu\text{L}$) was cast to improve film stability and anion-resistant permselectivity. Thus, the GO-MWCNTs/Nafion/GCE was obtained. For comparison, GO/GCE, and MWCNTs/GCE were prepared using the same procedures.

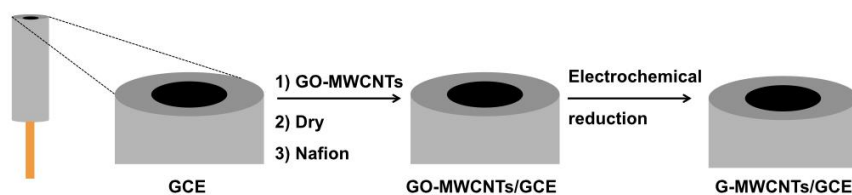


Figure 2.2. Procedure for the preparation of the graphene/MWCNTs/Nafion composite modified GCE electrode.

2.3 Synthesis of the phytic acid-polyaniline nanocomposite

Aniline (Aldrich) was freshly distilled over zinc dust to eliminate the oxidation impurities. The phytic acid-polyaniline (PA-PANI) nanocomposite was prepared using a “doping-dedoping-redoping”

method.⁵⁹⁻⁶¹ First, H_2SO_4 doped PANI nanofibers (H_2SO_4 -PANI) were synthesized according to the so-called rapid mixing polymerization method,⁶² followed by thorough dialysis. Second, H_2SO_4 -PANI was dedoped by immersing in a $\text{NH}_3\cdot\text{H}_2\text{O}$ solution (3%) for 12 h and the emeraldine base form of PANI (EB-PANI) was obtained. Finally, the EB-PANI was redoped in a phytic acid solution (0.05 mol L^{-1}) for 3 h under ultra-sonication to reach the maximum conductivity. This intermediate product was then sequentially dialyzed, filtered and dried in a vacuum chamber at 50°C , forming the final PA-PANI product. Stable dispersions of H_2SO_4 -PANI and PA-PANI solutions were obtained by ultrasonically dispersing the corresponding products in H_2SO_4 solution (0.01 mol L^{-1}) for 30 min. The procedures are shown in Figure 2.3.

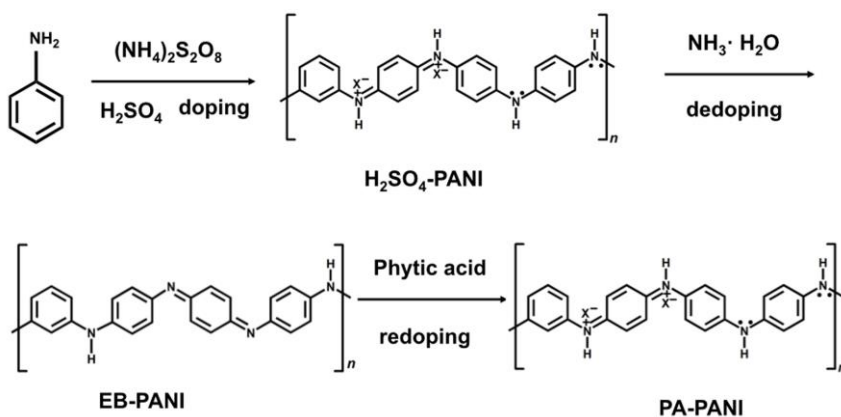


Figure 2.3. A schematic diagram showing the synthesis of phytic acid doped polyaniline nanofibers using the “doping-dedoping-redoping” method. X⁻ represents the counter ions in H_2SO_4 or phytic acid.

2.4 Fabrication of the phytic acid-polyaniline nanocomposite modified electrodes

Prior to use, the GCE was polished successively with the same steps as in section 2.2. Then, 5 μL of the PA-PANI solution (0.2 mg

mL⁻¹) was cast on the GCE surface, and dried under an infrared lamp. Next, 5 μ L of Nafion solution was cast on the electrode, forming the Nafion/PA-PANI/GCE. For comparison, Nafion/H₂SO₄-PANI/GCE electrodes were prepared using the same procedures.

2.5 Synthesis of the PDMS-silica nanocomposite

A PDMS-based polymer coating was prepared using hydroxyl terminated PDMS [Rhodosil Huile 48V, Bluestar Silicones with a weight-average molecular weight, M_w , of circa 80000 g/mol and a dynamic viscosity of 20 kg/(m·s) at 25 °C] as the prepolymer. Curing was achieved using the curing agent (heptadecafluoro-1,1,2,2-tetrahydrodecyl)-trimethoxysilane (Fluorochem Ltd.). The preparation steps are shown in Figure 2.4.

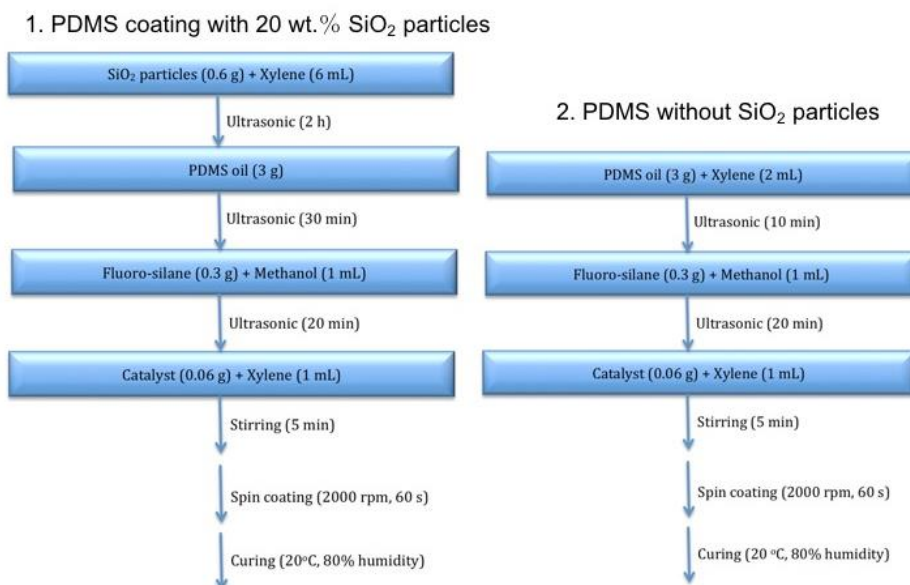


Figure 2.4. Preparation steps of PDMS coatings with and without silica nanoparticles.

The PDMS coating with 20 wt.% hydrophobic silica particles was prepared as follows. First, the hydrophobic silica nanoparticles (Aerosil R 972, Evonik, primary diameter of 16 nm) were suspended in xylene (95%, Sigma-Aldrich) and ultrasonically mixed. Next, the PDMS prepolymer was added into the particle dispersion, and the mixture was left to stir for 15 h using an impeller set to 85 rpm. Then, the curing agent was dissolved in methanol (99.8%, Sigma-Aldrich) and added to the mixture. Next, the catalyst dibutyltin diacetate (technical grade, Sigma-Aldrich) dissolved in 1 mL xylene was added. The uncured composite was quickly spin-coated onto silicon wafer substrates, which previously had been cut to size and cleaned with Piranha solution ($\text{H}_2\text{SO}_4 : \text{H}_2\text{O}_2$, 7 : 3) at 80 °C and Milli-Q water successively. The coated silicon wafer was cured at 80% relative humidity (20 °C) for one week. The pure PDMS coating without silica particles was prepared using the same steps except that xylene without silica particles was added to the PDMS base. The thickness of the PDMS coating is influenced by the spin coating speed and the viscosity of the PDMS prepolymer,⁶³ and the resulting thickness in our experiments was about 50–70 μm .

A schematic illustration of the curing reaction is shown in Figure 2.5. The polymerization proceeds via two steps: hydrolysis of the alkoxide groups on the curing agent followed by the water producing condensation reaction with the hydroxyl terminated PDMS.⁶⁴

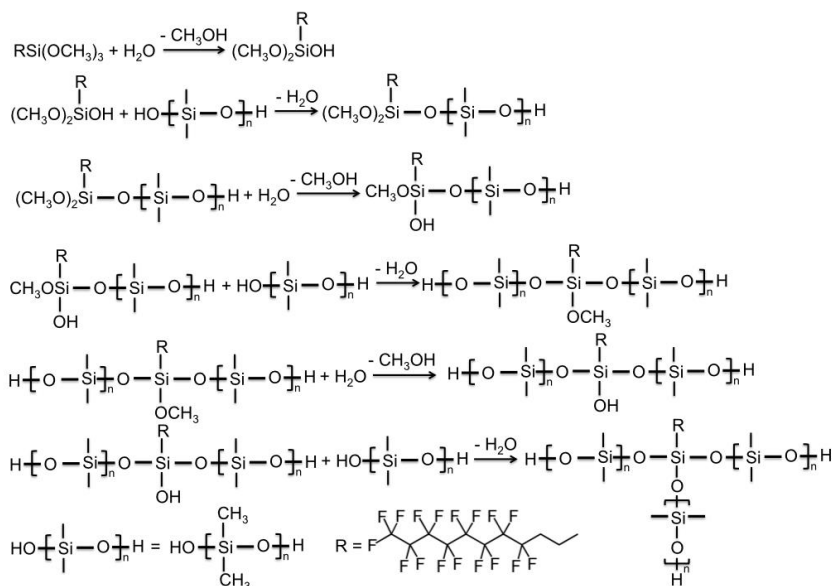


Figure 2.5. A schematic view of the curing reaction and the silicone network formed.

2.6 Synthesis of PEMA-PiBMA nanocomposite with hydrophobized silica nanoparticles

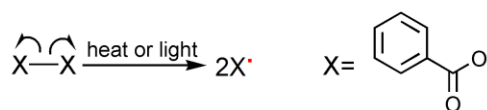
The polymer matrix used in this thesis is a quick curing acrylic resin system (ViaFix Struers), poly(ethyl methacrylate) (PEMA) white powder mixed with isobutyl methacrylate (iBMA) colorless liquid. The curing reaction of the system marked as PEMA-iBMA was achieved using benzoyl peroxide as the initiator and N,N-dimethyl-p-toluidine as the polymerization accelerator. The pure PEMA polymer used was analyzed by size exclusion chromatography (SEC) using tetrahydrofuran as the solvent, and had a M_w of circa 190 kg/mol. Other information about this acrylic resin system is available in Reference.^{65,66} Silica nanoparticles (> 99%, US Research Nanomaterials) with a primary particle diameter of 20–30 nm were used as fillers in the nanocomposite samples. For particle functionalization, dimethyldichlorosilane (> 99.5%, Sigma-Aldrich)

was used. The silanization process that renders the particle surface hydrophobic has been reported in a previous study.⁶⁷

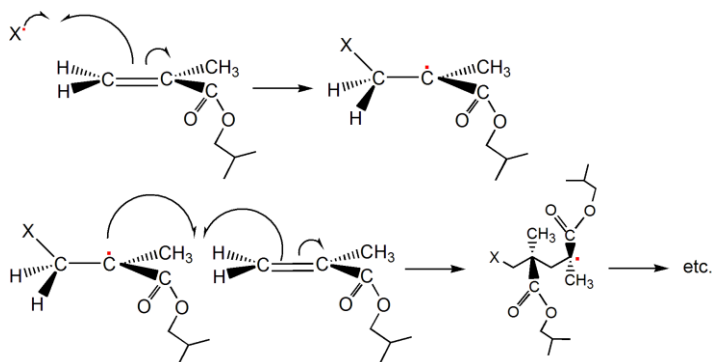
Two types of samples were prepared, i.e., pure PEMA-PiBMA thin films without particles and PEMA-PiBMA thin films with 15 vol% hydrophobized silica nanoparticles. The nanocomposite sample was made as follows: First, the silica nanoparticles (0.21 g) were ultrasonically dispersed into chloroform (99%, Sigma-Aldrich) for 1 h. Next, PEMA powder (2.2 g) was added into the particle sol and the mixture was continued to ultrasonic vibrate for 2 h. The mixture was put into a vacuum chamber at room temperature to remove part of the solvent, but in order to decrease the viscosity and obtain a smooth spin coating thin film, a small amount of solvent remained after this step. Finally, the iBMA liquid (1.8 g) was added and stirred quickly for 2 min. The mixture was quickly spin-coated at 1000 rpm for 60 s onto silicon wafer substrates that previously had been cut to size and cleaned with Piranha solution ($\text{H}_2\text{SO}_4 : \text{H}_2\text{O}_2$, 7 : 3) at 80 °C and Milli-Q water successively. The coated silicon wafer was cured in a vacuum chamber at 50 °C for 48 h. The pure polymer sample without silica particles was prepared using the same steps except that the PEMA polymer was dispersed into chloroform directly. The resulting samples are transparent and the thickness of the films used in our experiments was typically 50 μm .

A schematic of the polymerization reaction is illustrated in Figure 2.6. Polymerization of iBMA monomer in the presence of PEMA polymer is a free radical polymerization reaction,⁶⁸ which contains four steps as shown in Figure 2.6.

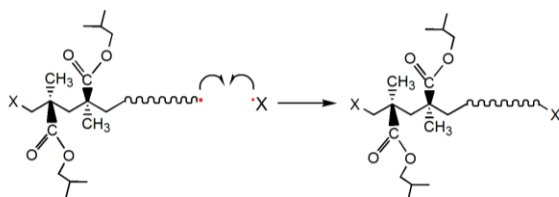
(a) Initiation



(b) Propagation



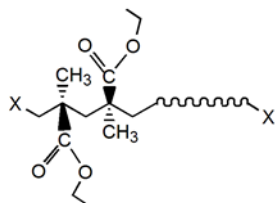
(c) Termination



The sample consists of two individual polymers:

-E-E-E-E-E- and -B-B-B-B-

where E represents ethyl methacrylate units, and B isobutyl methacrylate units. The structure of PEMA is:



(d) Chain transfer

The final polymer is a block copolymer of the type:

-E-E-E-E-E-B-B-B-B-

Figure 2.6. A schematic view of the polymerization reaction of the polymer matrix, poly(ethyl methacrylate) (PEMA)–poly(isobutyl methacrylate) (PiBMA) copolymer.

In the first step, the radical initiator, benzoyl peroxide, undergoes homolytic cleavage. In the propagation phase, the benzoyl radical ($X\bullet$ in Figure 2.6) adds to the double bond of ethylene, generating a

new organic radical. Successive ethylene molecules add to the growing polymer until termination occurs when two radicals combine. In Figure 2.6, the growing PiBMA polymer is terminated by a benzoyl radical, but in an alternative termination step two growing PiBMA radicals could also condense or be terminated via other reactions. In the chain transfer reaction, the added PEMA polymer still contains reactive free radicals, as a result, a block copolymer is formed. The propagation reaction and the chain transfer reaction are competitive. The produced polymer can be viewed as consisting of a tangle of “interpenetrating” polymer chains.⁶⁸ The PiBMA produced by radical polymerization is an amorphous thermoplastic with typical glass transition temperature, T_g , of approximately 50 °C.^{69,70} The T_g of PEMA is around 65 °C.^{69,71}

Chapter 3 Techniques

3.1 TEM and SEM

Transmission electron microscopy (TEM) is a powerful technique for material science, in which a high-energy beam of electrons is transmitted through an ultra-thin sample. The interactions between the electrons and the sample is used to investigate features such as the crystal structure, the dispersion of nanoparticles in nanocomposites and the microstructures within biological tissues. In **Paper I**, a JEOL JEM-1011 TEM with an accelerating voltage of 100 kV was used to characterize the morphology of the synthesized GO-MWCNTs thin layer.

Scanning electron microscopy (SEM) creates an image of a sample by scanning a focused beam of high-energy electrons. The electrons interact with the sample, generating a variety of signals that contain information about the surface morphology and chemical composition. In **Paper II**, SEM (Hitachi, JEOL JSM-6700F) with an accelerating voltage of 5 kV was employed to characterize the topography of as-prepared PANI nanofibers. Specimens of PANI are electrically conductive; no coating was deposited on the sample surface.

3.2 EDS analysis

Energy dispersive spectroscopy (EDS) is one of the most commonly used elemental analysis techniques. It involves the generation of an X-ray spectrum detecting elements from atomic number 4 to 92, which takes advantage of the principle that each element has a unique atomic structure providing different element peaks or distribution. In **Paper II**, the incorporation of phytic acid into the PANI chains was evidenced using EDS equipped on a SEM.

3.3 Raman spectroscopy

Raman spectroscopy is a fast and convenient nondestructive technique to identify the ordered and disordered structure of carbon. In **Paper I**, the electronic structure of carbon materials (MWCNTs, graphene oxide and GO-MWCNTs) was characterized with Raman spectroscopy. The Raman spectra of carbon materials have been demonstrated to show characteristic peaks at 1350 cm^{-1} (D band), 1580 cm^{-1} (G band) and 2700 cm^{-1} (2D band).⁷² The D band is the defect peak near 1350 cm^{-1} , which reflects the randomness of graphite layers, such as the amorphous carbon or specific vibrations at the edges that can break the symmetry rule. The G band located at 1580 cm^{-1} is usually assigned to the characteristic band of E_{2g} phonon of sp^2 carbon atoms, indicating the extent of crystallization and symmetry of carbon based materials. The 2D band (also called as G' band) at around 2700 cm^{-1} derives from two-phonon inelastic scattering.⁷²

3.4 FT-IR spectroscopy

Fourier transform infrared spectroscopy (FT-IR) is used to obtain an infrared absorption or emission spectrum of a sample. This technique is widely used in polymer science, organic synthesis, pharmaceutical industry and food analysis. The infrared-rays cover the wavenumber range from about 12800 to 10 cm^{-1} . In **Paper II** and **Paper III**, FT-IR was employed to study the chemical compositions of as-prepared PANI based nanocomposites.

3.5 Open-circuit potential, OCP

Open-circuit potential (OCP) measurements are widely used to study corrosion processes. OCP refers to the difference of electrical

potential between two electrode terminals when detached from a circuit at zero current. For a coating/metal system, the corrosion reaction at open-circuit conditions takes place due to the local formation of anodes and cathodes on the metal surface. OCP is important since a metal with lower OCP normally will degrade faster in the electrolyte than a metal with higher OCP. In **Paper III**, the change of OCP vs. exposure time was used to evaluate the long-term protective properties by the composite coating.

3.6 Atomic force microscopy, AFM

3.6.1 Tapping mode

Tapping mode AFM, also known as amplitude modulation atomic force microscopy (AM-AFM), is currently the dominant dynamic AFM technique. It allows characterization of topography and it also provides some information on surface mechanical properties via the phase image. A cantilever is excited near its resonance frequency, and during the oscillation it intermittently contacts the sample surface. The amplitude of the oscillation is thereby reduced, and the amplitude-reduction is kept constant by the feedback system to provide a topographic image. The phase difference between the driving voltage and the cantilever response is also recorded, providing a phase image that is affected by material properties such as surface viscoelasticity and tip-sample adhesion. The main drawback of the tapping mode technique is that it is practically impossible to correlate the measured phase, which gives a measure of cantilever energy dissipation, to quantitative mechanical properties of the surface. The value of the phase shift is influenced by experimental parameters such as amplitude setpoint and tapping frequency, and it depends in a complex way on the tip-surface interactions.

Rectangular cantilevers with nominal dimensions of 125 μm in length and 40 μm in width (BudgetSensors Tap300Al-G, spring constant of about 40 N/m, tip radius < 10 nm as specified by the manufacturer) were used to perform the tapping mode experiments in **Paper IV**.

3.6.2 Intermodulation AFM

Intermodulation AFM (ImAFM) is a newly developed multi-frequency dynamic AFM technique, which has been described in detail in the literature.⁷³ The key feature is that the cantilever is simultaneously excited with two frequencies (f_1 and f_2) close to the resonance frequency. When the cantilever motion is perturbed by the non-linear tip-surface interaction, the two drive frequencies will mix and new frequencies (f_{IMP}), known as intermodulation products (IMP), near the resonance appear in the response. These intermodulation products occur at specific values of frequency given by:

$$f_{\text{IMP}} = mf_1 + nf_2 \quad (3.1)$$

where m and n are integers (positive or negative), and $|n| + |m|$ is the order of the intermodulation product.⁷⁴

The intermodulation products, measured with a lock-in amplifier, contain information on tip-surface interactions and thereby surface mechanical properties.^{75,76} The amplitude and phase of each intermodulation product is recorded at every image pixel in real time while scanning.

The multi-frequency intermodulation response can be directly transformed into two force-quadrature curves which display the integrated forces over each single oscillation cycle of amplitude A . This integral force is resolved as two components: one is in-phase

with the cantilever oscillation, $F_I(A)$, and the other is quadrature to the oscillation (in-phase with the velocity), $F_Q(A)$. (This is similar to the splitting of the complex impedance into its real and imaginary part, and the splitting of an oscillatory rheological response into a storage modulus and a loss modulus.) The conservative part of the tip-surface interaction is a function of the tip position only, as in contact mechanics. In this case, the force vs. tip position curve can be directly reconstructed (i.e. without invoking any model) from $F_I(A)$ using the inverse Abel transform.⁷³ Such a force curve would correspond to that measured by quasi-static methods typically used in AFM force curve analysis.

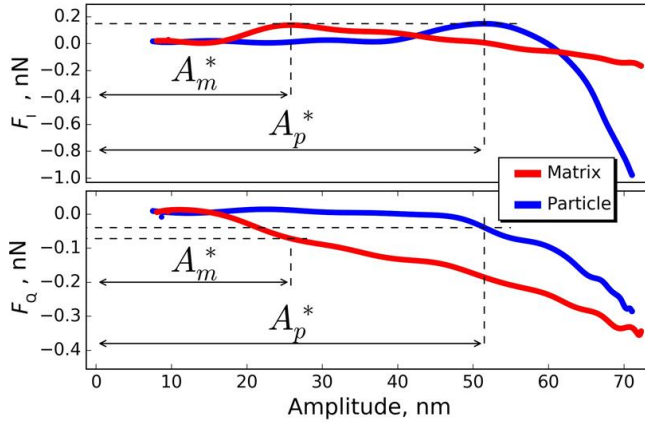


Figure 3.1. $F_I(A)$ and $F_Q(A)$ curves reconstructed for the tip-surface interaction on the polymer matrix (red) and over an embedded silica particle (blue) as measured with ImAFM. A_m^* and A_p^* correspond to the amplitudes at maximum attractive force on the $F_I(A)$ curve, and can be viewed as the tip-surface contact point. Note that a net attractive $F_I(A)$ has positive sign and a net repulsive one negative sign.

The dissipated energy, E_{dis} , is the work done by the tip-surface force for each oscillation cycle. It can directly be obtained from the following relation.

$$E_{\text{dis}}(A) = -2\pi A \cdot F_Q(A) \quad (3.2)$$

Paper IV is particularly focused on the energy dissipated at the maximum of the $F_1(A)$ curve, occurring at the amplitude $A = A^*$ (Figure 3.1).^{73,77}

ImAFM measurements were performed on the Bruker Dimension Icon AFM connected to a multi-frequency lock-in amplifier (Intermodulation Products AB, Sweden), which generates the drive signals and records the intermodulation spectra. The IMP software suite (Version 1.1, Intermodulation Products AB) and in-house written scripts incorporated within the IMP software suit were used to analyze the data. All experiments were performed in ambient air. The same type of cantilevers as used in tapping mode was used to perform ImAFM experiments. The spring constant of each cantilever was determined with the non-invasive thermal noise method, where the calibration can be traced back to one noise spectrum, as implemented in the ImAFM Software Suite (Intermodulation Products AB, Sweden).^{78,79}

3.6.3 Force mapping and QI AFM

In force mapping measurements, a force curve is recorded at every image pixel keeping the maximum vertical cantilever deflection constant, whereby building a map of the tip-sample interaction. By analyzing the force curves measured at each pixel, various surface mechanical properties can be extracted. Quantitative Imaging mode (QI AFM), similar to force mapping mode, allows simultaneous collection of data on surface morphology and mechanical properties at a controllable vertical force without applying any significant lateral force.⁸⁰ The main difference between QI and force mapping lies in the algorithm of the tip motion and the force curve collection rate (333 Hz in QI mode and 20 Hz in force mapping mode were used in this thesis). Slope or stiffness, tip-

sample adhesion force and work of adhesion can be determined directly from the force curves without using any models (Figure 3.2).

The linear fitting region for slope/stiffness on the approach curve is illustrated in the inset of Figure 3.2 on an expanded scale. The slope/stiffness value is calculated by $(\Delta y/\Delta x)$, where Δy is the change of cantilever vertical deflection in nm and Δx is the change in separation distance in μm , thus the resulting unit of the slope/stiffness is nm/ μm . The fitting region along the x-axis (Δx) used in my thesis was from final contact and 5 nm out. The maximum adhesion force is determined by the minimum point on the retract force curve, and the work of adhesion is calculated by the area enclosed by the retract force curve and the x-axis (shaded region in the main figure of Figure 3.2).

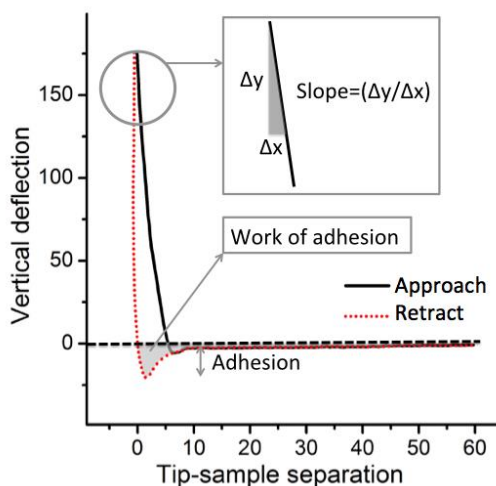


Figure 3.2. A schematic illustration of the analysis of the force curves in the QI and force mapping spectroscopy AFM modes (the numbers on the axes are shown as an illustration). The linear fitting region for slope/stiffness on the approach curve is illustrated in the inset on an expanded scale. The maximum adhesion force is determined by the minimum point on the retract force curve. Work of adhesion is calculated from the area enclosed by the retract force curve and the x-axis (shaded region in the main figure).

In **Paper V**, a JPK NanoWizard® 3 AFM (JPK Instruments AG, Berlin, Germany) was used to perform QI and force mapping spectroscopy measurements. All experiments were performed in air. The temperature was controlled via the JPK High Temperature Heating Stage (HCS™). The actual temperature on the sample surface was measured using a temperature sensor (Digital precision thermometer, TD 10, with a probe, TKS 200; VWR Collection). A second order polynomial-flattening algorithm was employed to remove surface tilt from height images. In order to quantify the measured force, the exact value of the spring constant was determined by the Sader method.^{81,82}

Chapter 4 Key results and discussions

The overall aims of this thesis work are to synthesize nanomaterials based composites and explore their applications in electrochemical sensors and for corrosion protection. In the Section 4.1 I focus on the synthesized graphene-MWCNTs nanocomposite and its application. In Section 4.2 the synthesized phytic acid-PANI nanocomposite and its application are investigated. Next, the alkyd-PANI composite coating is discussed in Section 4.3. Finally, in Section 4.4 the local surface mechanical properties of nanocomposites are discussed.

4.1 Electrochemical application of synthesized graphene-MWCNTs nanocomposites

4.1.1 Morphology, molecular and electronic structures

The morphology of the synthesized GO-MWCNTs was characterized by TEM. Figure 4.1a shows that MWCNTs nanofibers, with the length of about 0.5–2 μm , are well dispersed on the GO nanolayers. At the same time, the GO nanolayers exhibit large and unfolded planar structures.

The molecular and electronic structures of the nanomaterials were characterized with UV-vis spectroscopy and Raman spectroscopy, respectively. UV-vis results of as-prepared MWCNTs, GO and GO-MWCNTs are displayed in Figure 4.1b. i) GO is observed to exhibit two peaks: a strong peak at around 220–230 nm and a shoulder peak at 300 nm, which are assigned to the π – π^* transition of C–C bonds and n– π^* transition of carbonyl groups, respectively. ii) MWCNTs exhibit a broad and weak π – π^* transition peak at 225 nm, which is due to a small proportion of water-soluble MWCNTs, since the hydrophilicity of MWCNTs has increased after acid treatment.

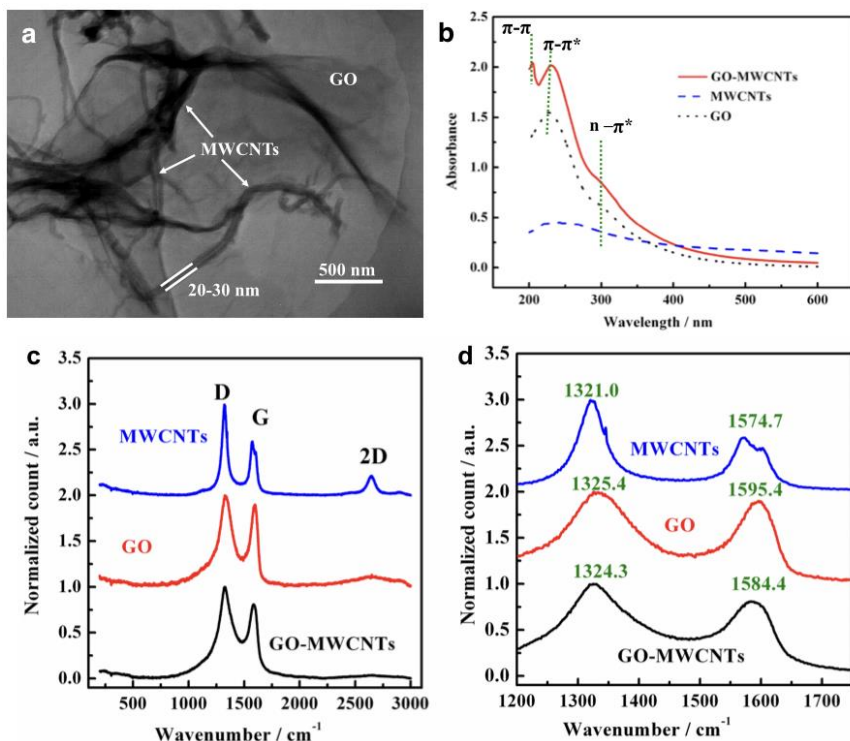


Figure 4.1. (a) A low magnification TEM image of GO-MWCNTs. The arrows point to the MWCNTs. (b) UV-Vis absorption spectra of GO (dotted line), MWCNTs (dashed line) and GO-MWCNTs (solid line) dispersions. (c) Comparison of Raman spectra of MWCNTs, GO and GO-MWCNTs. They are scaled to have the same height of the D peak at about 1350 cm⁻¹. (d) Magnification of D band and G band in the wavenumber range from 1200 cm⁻¹ to 1700 cm⁻¹.

iii) Compared with GO and MWCNTs, a new peak at 205 nm is observed for the GO-MWCNTs nanocomposite, which is assigned to the π - π covalent interaction between the GO nanosheets and the sidewalls of MWCNTs via the π -conjugated aromatic rings on both GO and MWCNTs.

The full and locally expanded Raman spectra of MWCNTs, GO and GO-MWCNTs are shown in Figure 4.1(c, d). The Raman spectrum of MWCNTs exhibits a strong D band at 1321.0 cm⁻¹, a moderate G band at 1574.7 cm⁻¹, and a weak 2D band at 2648.6 cm⁻¹. The Raman spectrum of GO shows similar intensity peaks of the D band and G

band. Compared with MWCNTs, the intensity of G band for GO is much stronger. However, the Raman spectrum of GO shows a much weaker and broadened 2D peak than that of MWCNTs, suggesting that considerable defects exist in the as-synthesized GO films. Strong D and G bands are observed for GO-MWCNTs; however, the peak positions of D and G bands are located at lower frequency relative to that of GO, i.e., the D and G band peaks are red-shifted. From Figure 4.1d, it is observed that the D band is red-shifted by 1.1 cm^{-1} , meanwhile, the G band is red-shifted by 11.4 cm^{-1} . Particularly, the 2D band disappears in the GO-MWCNTs hybrid nanomaterials, revealing that i) new structural defects were formed in the GO-MWCNTs nanocomposite and ii) the combination of one-dimensional CNTs with two-dimensional graphene to a certain extent produced three-dimensional carbon networks.

Furthermore, the ratios of the peak area of the D band to that of the G band, i.e. I_D/I_G , are calculated for MWCNTs, GO and GO-MWCNTs. The ratio of GO-MWCNTs ($I_D/I_G = 1.2$) is in between that found for GO ($I_D/I_G = 1.1$) and MWCNTs ($I_D/I_G = 1.7$), implying that GO and MWCNTs co-exist in the nanomaterials. Therefore, one can conclude that the GO-MWCNTs hybrid material was successfully fabricated.

4.1.2 Electrochemical properties

The electrochemical reduction properties of GO-MWCNTs nanocomposites and GO were investigated in a potential window from 0 V to -1.7 V using CV, and some data are shown in Figure 4.2. The onset potential for the electrochemical reduction of GO is -0.85 V and the complete reduction of GO needs more than 10 voltammetric cycles. In comparison, the onset potential for the electrochemical reduction of GO-MWCNTs nanocomposites is -0.45 V , significantly less negative than that of the GO. In addition, the

complete electrochemical reduction of GO-MWCNTs needs just three voltammetric cycles. The results illustrate the good conductivity of CNTs promotes the reduction of GO. CNTs may act as conducting wires that connect the different GO sheets and accelerate the electron transfer rate from one GO sheet to another, thereby making it more easy to reduce the GO components in the hybrid nanocomposite.

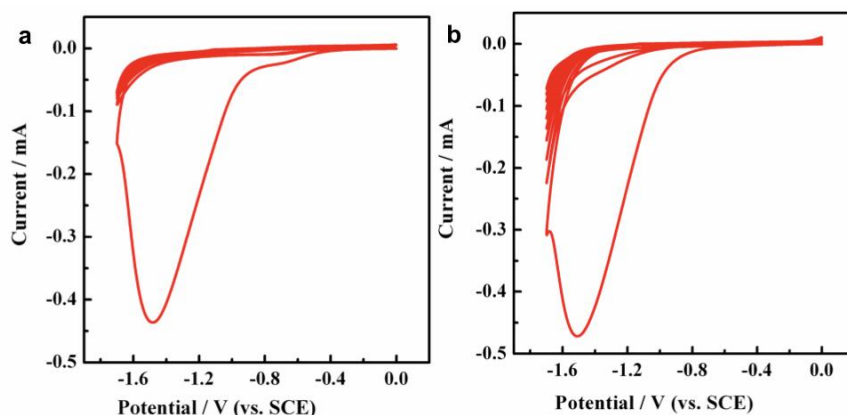


Figure 4.2. The first 10 cyclic voltammograms (CVs) at a scan rate of 50 mV s⁻¹ for the electrochemical reduction of GO-MWCNTs modified GCE (a) and GO modified GCE (b) in 0.1 M HAc-NaAc buffer solution (pH 4.5) saturated with nitrogen gas. The initial potential is 0.0 V.

The charge transfer rate at the electrode/solution interface was further studied by CV, comparing the charge-transfer rates at the bare GCE and GO-, MWCNTs- and G-MWCNTs-modified GCEs using the [Fe(CN)₆]^{3-/4-} couple as a redox probe. The results are shown in Figure 4.3. The cyclic voltammogram of a bare GCE, MWCNTs- and G-MWCNTs-modified electrodes all show quasi-reversible redox properties, as demonstrated by the peak potential differences (ΔE_p) of about 80 mV and the ratios between anodic and cathodic peak currents of about 1:1, indicating that the GCE, MWCNTs- and G-MWCNTs-modified electrodes were all good reaction interfaces for

the $[\text{Fe}(\text{CN})_6]^{3-/4-}$ couple. In addition, the anodic and cathodic peak currents were the highest at the G-MWCNTs-modified electrode under the same conditions, i.e., the charge transfer at G-MWCNTs-modified electrode was the most rapid, which is attributed to the synergistic effect of graphene and MWCNTs. For the GO-modified GCE, both the anodic and cathodic peak currents were lowered significantly due to the poor conductivity of GO.

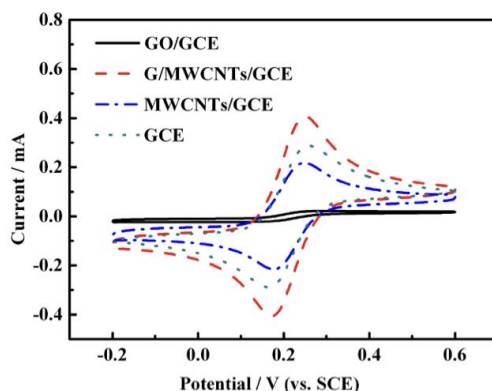


Figure 4.3. Cyclic voltammograms of modified and unmodified GCEs in 0.1 M KCl solution containing 5 mM $\text{K}_3\text{Fe}(\text{CN})_6$ + 5 mM $\text{K}_4\text{Fe}(\text{CN})_6$ at a scan rate of 50 mV s^{-1} .

4.1.3 Electrochemical response to heavy metal ions

To obtain the best electrochemical response for Pb^{2+} and Cd^{2+} ions, the detection conditions were first optimized. The influence of buffer solution pH on the stripping peak currents was investigated in the pH range from 3.5 to 5.5, and pH 4.5 was chosen as the optimal pH for analysis. The influence of the deposition potential on the stripping peak currents was studied in the range from -0.9 V to -1.5 V and a deposition potential of -1.4 V was selected. A deposition time of 180 s was selected as a compromise between practical measurement time and high sensitivity.

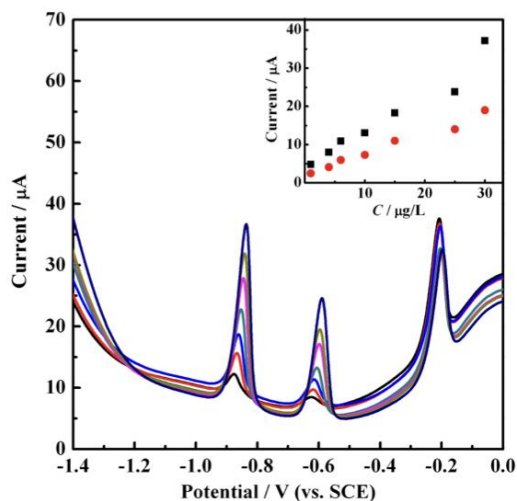


Figure 4.4. DPASV stripping signals for various concentrations (0.5, 5.0, 7.0, 10, 15, 25, and 30 $\mu g L^{-1}$ from bottom to top) of Pb^{2+} and Cd^{2+} ions on the bismuth and Nafion films modified G/MWCNTs/GCE. Inset shows the calibration curves of Pb^{2+} and Cd^{2+} ions. Supporting electrolyte: 0.1 M acetate buffer (pH 4.5) containing 500 $\mu g L^{-1}$ Bi^{3+} ; deposition potential: -1.4 V; deposition time: 180 s; amplitude: 50 mV; increment potential: 5 mV; quiet time: 10 s.

The detection results for different concentrations of Pb^{2+} and Cd^{2+} ions under these optimized conditions are shown in Figure 4.4. The resulting calibration plot (see inset) for Pb^{2+} is observed to be linear over the concentration range from 0.5 $\mu g L^{-1}$ to 30 $\mu g L^{-1}$. The equation of the calibration curve is $I_p = 0.1914c + 1.6709$ with the correlation coefficient of $R = 0.978$, where I_p is the stripping peak current (μA), and c is the concentration ($\mu g L^{-1}$). The limit of detection is 0.2 $\mu g L^{-1}$ ($S/N = 3$) in the case of a deposition time of 180 s, which is lower than the recommended value of 10 $\mu g L^{-1}$ for Pb^{2+} in drinking water given by the World Health Organization (WHO). Similarly, the calibration plot for Cd^{2+} ranges from 0.5 $\mu g L^{-1}$ to 30 $\mu g L^{-1}$. The equation of the calibration curve is $I_p = 0.2358c + 2.0457$ ($R = 0.983$). The limit of detection is 0.1 $\mu g L^{-1}$ ($S/N = 3$) in

the case of a deposition time of 180 s. The guideline value is $3 \mu\text{g L}^{-1}$ for Cd^{2+} in drinking water given by the WHO.

4.2 Electrochemical application of synthesized phytic acid-PANI nanocomposite

4.2.1 Morphology and molecular structure

The morphology of the synthesized nanofibers was characterized using SEM and the results are shown in Figure 4.5. Well-defined nanofibered structures of the H_2SO_4 -PANI are shown in a low-magnification SEM picture (Figure 4.5a). The diameter of the fibers is about 40–60 nm and the length is 0.5–2 μm . A higher magnification SEM image shows that the H_2SO_4 -PANI nanofibers are closely reticulated with each other, forming a continuous network (Figure 4.5b). The as-synthesized PA-PANI also keeps the expanded nanofibered structure shown in Figure 4.5(c, d), however, it displays a shorter length and a more porous network. This porous composition is due to the effect of phytic acid on the orientation of PANI chains. And the porous structure possesses higher specific surface area, thus offering a more advantageous geometry for interacting with the Cd^{2+} and Pb^{2+} ions during the ASV analysis.

In addition, EDS spectra of H_2SO_4 -PANI and PA-PANI nanofibers are shown in Figure 4.5e and Figure 4.5f, respectively. The EDS spectrum of H_2SO_4 doped PANI nanofibers demonstrates four typical peaks for C, N, O and S elements, respectively. In comparison, the EDS spectrum of phytic acid doped PANI shows peaks for C, N, O and P elements. The presence of the strong P peak at about 2 keV in Figure 4.5f certifies that phytic acid was successfully incorporated into the PANI framework.

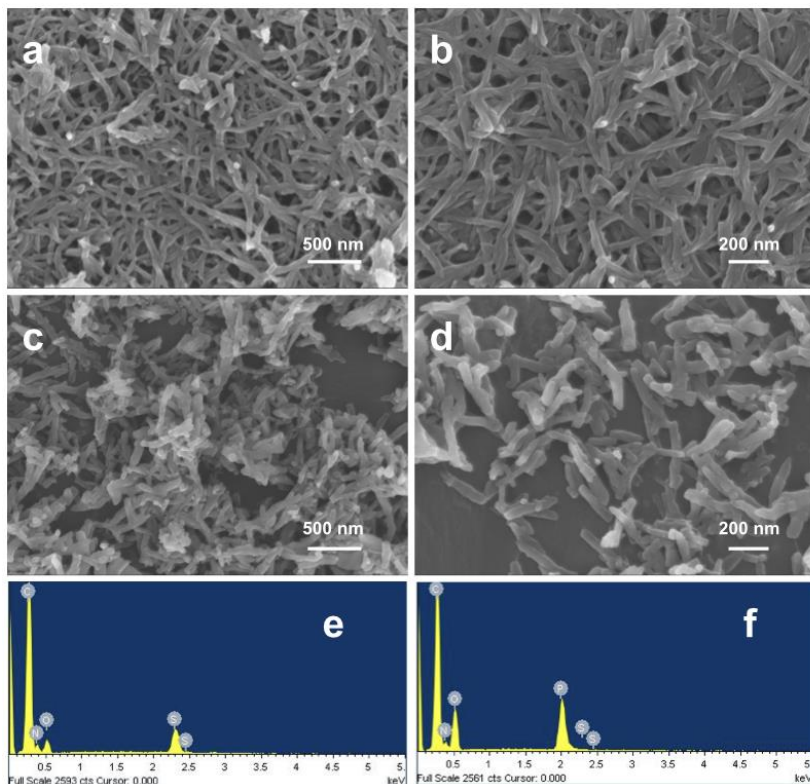


Figure 4.5. (a, b) SEM images of H_2SO_4 doped polyaniline nanofibers and (c, d) phytic acid doped polyaniline nanofibers. (e, f) The corresponding EDS spectra of the two kinds of nanofibers. Note the P-peak at about 2 keV in panel f and the S-peak at 2.3 keV in panel e.

The molecular structures of as-prepared PA-PANI and H_2SO_4 -PANI nanomaterials were investigated by FT-IR spectroscopy (Figure 4.6). The characteristic peaks for H_2SO_4 -PANI nanofibers and the corresponding structures are summarized in Table 1. All the peaks together indicate that the protonated PANI nanofibers are in the emeraldine salt form. The peak at 1139 cm^{-1} was regarded as a characteristic peak showing the electron delocalization degree in PANI.

Compared with H_2SO_4 -PANI nanofibers, PA-PANI nanofibers demonstrate roughly identical peak intensity. However, the peak positions are red-shifted. For example, the C-N stretching vibration

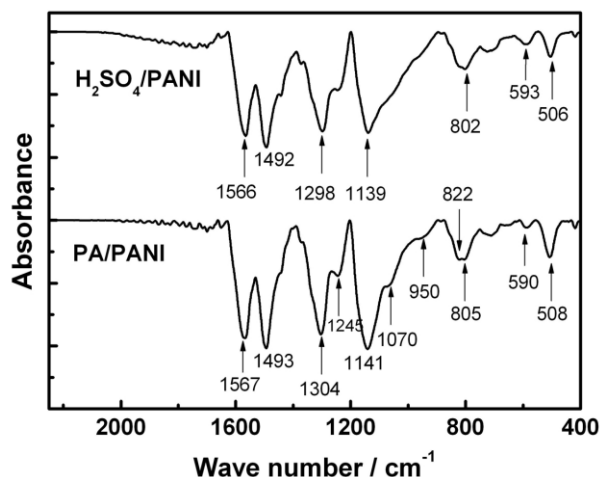


Figure 4.6. FT-IR spectra of H_2SO_4 doped polyaniline nanofibers and phytic acid doped polyaniline nanofibers.

Table 1

FT-IR peaks for H_2SO_4 doped polyaniline nanofibers and the corresponding structures.

Peaks (cm^{-1})	Corresponding structures
1566	C=C stretching vibrations of the quinoid ring (Q)
1492	C=C stretching vibrations of the benzenoid ring (B)
1298	C-N stretching vibrations of secondary aromatic amines
1139	the in-plane aromatic C-H bending
802	C-H bending vibrations of the 1, 4-disubstituted aromatic rings
506	

peak is red-shifted from 1298 cm^{-1} to 1304 cm^{-1} and the in-plane aromatic C-H bending vibration peak is red-shifted from 1139 cm^{-1} to 1141 cm^{-1} , which are due to the introduction of phytic acid. Furthermore, the relative peak intensity at 1141 cm^{-1} is increased, representing an increased conductivity of the PA-PANI nanofibers

since this peak is originating from the in-plane aromatic C–H bending. The integration of phytic acid into the PANI framework is also evidenced by comparing the absorption peaks i) at 1070 cm^{-1} which is due to the vibration of P–OH bonds; ii) at 950 cm^{-1} and 822 cm^{-1} which are assigned to the vibration of P–O–C bonds; and iii) the enhanced peak at 1245 cm^{-1} which is due to the vibration of P=O bonds. These peaks are all representative peaks for phytic acid.

4.2.2 Electrochemical properties

The charge transfer rate at the electrode/solution interface was studied by electrochemical impedance spectroscopy (EIS). Figure 4.7 shows a set of Nyquist curves for bare GCE, H_2SO_4 -PANI and PA-PANI functionalized GCEs. Compared to the bare GCE, very small charge transfer resistances (R_{ct} , small semicircle in the high frequency region) were observed on the H_2SO_4 -PANI and PA-PANI

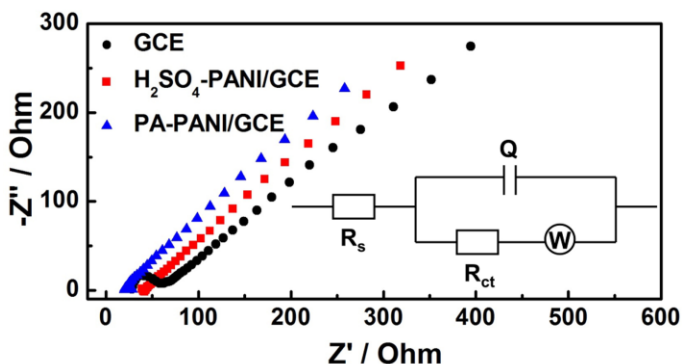


Figure 4.7. A Nyquist diagram of electrochemical impedance spectra obtained at GCE, H_2SO_4 -PANI/GCE, PA-PANI/GCE electrodes in a solution of 5 mM $\text{K}_3\text{Fe}(\text{CN})_6$, 5 mM $\text{K}_4\text{Fe}(\text{CN})_6$ and 1.0 M KCl. Inset: an equivalent circuit describing the electrode-solution interface, where R_{ct} is the ionic transfer resistance, R_s is the solution resistance, Q is the constant phase element, and W is the Warburg impedance of diffusion ions.

modified electrodes. A simple equivalent circuit was used to fit the spectra (see the inset). The simulated R_{ct} values for the bare GCE, H_2SO_4 -PANI/GCE and PA-PANI/GCE electrodes are $40.0 \Omega \cdot cm^2$, $9.55 \Omega \cdot cm^2$ and $7.22 \Omega \cdot cm^2$, respectively, indicating that the PA-PANI nanocomposite reduces the energy barrier for the mass transfer most significantly, and increases the charge transfer rate at the electrode/electrolyte interface.

4.2.3 Electrochemical response to heavy metal ions

To reveal the detection performance of the nanocomposite upon exposure to metal ions, the DPASV curves for Nafion/ H_2SO_4 -PANI and Nafion/PA-PANI modified electrodes were determined in the same electrolyte containing $15 \mu g L^{-1}$ of both Cd^{2+} and Pb^{2+} . The results are shown in Figure 4.8. It is obvious that increased stripping currents for both Cd^{2+} and Pb^{2+} were obtained on the PA-PANI

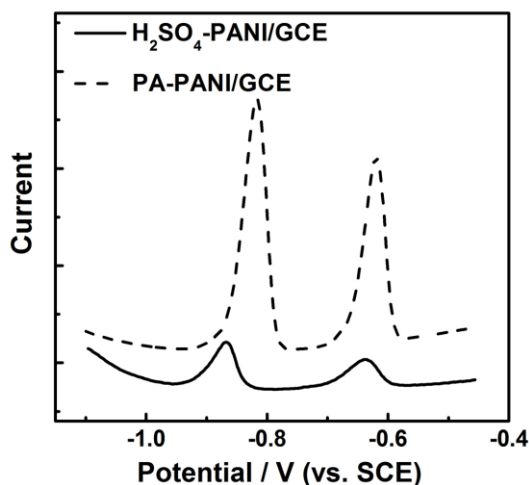


Figure 4.8. DPASV curves of $15 \mu g L^{-1}$ of Cd^{2+} and Pb^{2+} at the Nafion/ H_2SO_4 -PANI/GCE and Nafion/PA-PANI/GCE electrodes. DPASV conditions: acetate buffer (pH 4.0) containing $400 \mu g L^{-1} Bi^{3+}$, deposition potential of $-1.2 V$, deposition time of 180 s, amplitude of 50 mV, and quiet time of 20 s.

modified electrode. The enhanced current signal is due to i) the introduction of $-\text{PO}_3\text{H}_2$ groups, which is advantageous for the preconcentration of Cd^{2+} and Pb^{2+} ions, and ii) the enhanced conductivity, which is beneficial to the charge transfer of metal ions at the electrode/solution interface. In addition, the stripping peaks at PA-PANI modified GCE are slightly shifted to less negative potential, which is maybe due to the strong interaction between phytic acid and heavy metal ions.

The detecting conditions were first optimized to obtain the best stripping responses for heavy metal ions by taking into account the overall measurement time and sensitivity. Under these optimized conditions (listed in the caption of Figure 4.8), the simultaneous detection of Cd^{2+} and Pb^{2+} was performed at the Nafion/PA-PANI modified electrode. The results are displayed in Figure 4.9. The stripping currents vs. potential were shown in a concentration range from 0.05 to 60 $\mu\text{g L}^{-1}$ for Cd^{2+} and Pb^{2+} (Figure 4.9a). Well-resolved and sharp peaks were acquired. From Figure 4.9b, it is observed that the peak currents increased linearly with increasing metal ion concentrations. The calibration curve for Cd^{2+} was linear in the concentration range 0.05–60 $\mu\text{g L}^{-1}$ and for Pb^{2+} it was linear in the concentration range 0.1–60 $\mu\text{g L}^{-1}$. The corresponding linear equations for Cd^{2+} and Pb^{2+} were $I_p = 0.9216c (\text{Cd}^{2+}) - 0.6447$ ($R^2 = 0.992$) and $I_p = 0.6597c (\text{Pb}^{2+}) - 0.1659$ ($R^2 = 0.995$), respectively. The detection limits were 0.02 $\mu\text{g L}^{-1}$ and 0.05 $\mu\text{g L}^{-1}$ for Cd^{2+} and Pb^{2+} ($S/N = 3$), respectively. These limits of detection are far below the guideline values in drinking water given by the WHO, i.e. 10 $\mu\text{g L}^{-1}$ for Pb^{2+} and 3 $\mu\text{g L}^{-1}$ for Cd^{2+} . Compared with the method proposed in section 4.1, the Nafion/PA-PANI modified electrode shows much lower limits of detection and wider detection ranges than those of Nafion/G-MWCNTs modified electrode. This is maybe due to the lower background current obtained here.

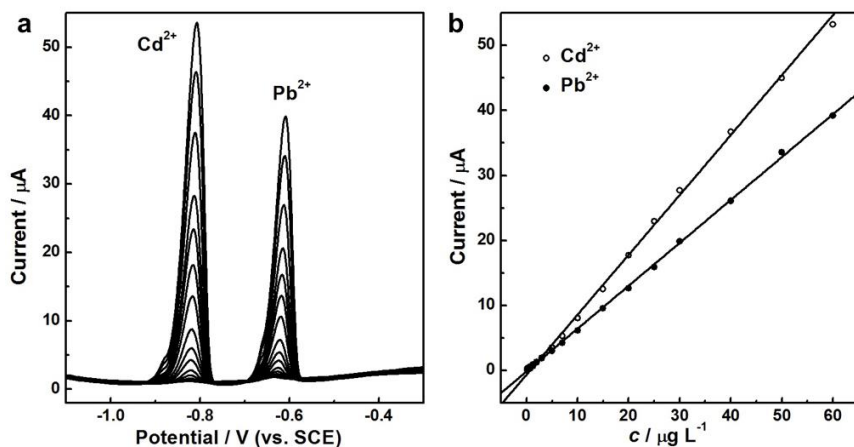


Figure 4.9. (a) DPASV stripping signals and (b) the calibration curves for different concentrations of Cd^{2+} and Pb^{2+} (0.05, 0.1, 0.5, 1.0, 2.5, 5.0, 7.5, 10.0, 15.0, 20.0, 25.0, 30.0, 40.0, 50.0, 60.0 $\mu\text{g L}^{-1}$ from bottom to top) at the Nafion/PA-PANI/GCE electrode. DPASV conditions are the same with those displayed in **Figure 4.8**.

The PA-PANI modified electrode was further employed to determine heavy metal ions in actual water samples taken from three different sources. All samples were filtered with a 0.22 μm membrane filter, followed by addition of a 0.1 mol L^{-1} acetate buffer solution (pH 4.0) containing 400 $\mu\text{g L}^{-1}$ Bi^{3+} ions. The results obtained by standard addition method (1.0 $\mu\text{g L}^{-1}$ of Cd^{2+} and Pb^{2+} were added) are reported in Table 2. Good recovery rates were gained for all three samples.

Table 2

Determination of Cd^{2+} and Pb^{2+} in actual water samples.

Sample	Recovery of Cd^{2+} (%)	Recovery of Pb^{2+} (%)
Tap water	95.9	105.2
Waste water	103.2	98.4
River water	107.1	94.6

4.3 Electrochemical application of the PANI-alkyd nano-composite

4.3.1 Morphology

The morphology of the alkyd coatings was characterized with SEM and the results are shown in Figure 4.10. The SEM cross-section image of the alkyd coating without PANI (Figure 4.10a) shows a wave-like feature, which is due to the microtome cutting, and no particles or aggregates are observed. By comparison, the SEM images of the composite coating with PANI demonstrate different features (Figure 4.10b), a large 1 μm -sized PANI aggregate could be observed. In addition, a higher magnification SEM image of the composite coating in Figure 4.10c shows PANI nanoparticles distributed uniformly in the polymer matrix.

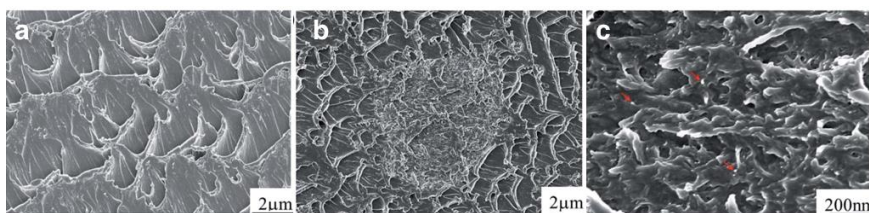


Figure 4.10. SEM cross-section images of the alkyd coatings without (a) and with 1 wt.% PANI (b, c). The red arrows in panel c point towards PANI nanoparticles.

4.3.2 Electrochemical evaluation of long-term anticorrosion performance

The inserted images in Figure 4.11 show photos of the samples taken during immersion in 3 wt.% NaCl. The carbon steel coated with alkyd without PANI showed visible red rust over the entire exposed area after 4 days. This is due to the limited barrier-type of corrosion protection offered by the alkyd coating, and the

penetration of water and ions occurs readily. However, the carbon steel coated with the composite coating showed only a few small corrosion sites after 40 days' exposure, which indicated significantly improved protective properties by the added PANI nanoparticles. These different performances were evaluated by the open-circuit potential (OCP) vs. time of exposure tests in 3 wt.% NaCl solution. For the composite coating, during the early stage of exposure, the OCP dropped to some extent for three times, but an increase was followed after each drop. However, for the reference sample, modest increase was repeated only two times. The considerably higher OCP value finally obtained on the composite sample suggests passivation of the carbon steel by the redox reaction of the PANI component. Therefore, the steel surface with defects becomes oxidized while the covered PANI is reduced, which is a self-healing effect provided by the PANI.

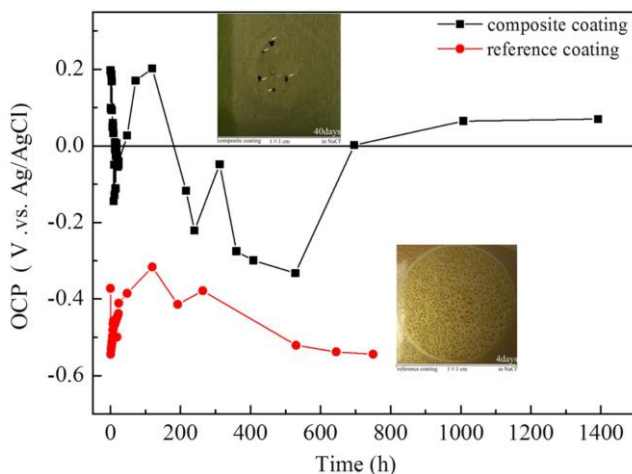


Figure 4.11. Variations of the open-circuit potential (OCP) vs. time of exposure for the alkyd coatings without and with 1 wt.% PANI composite coating on carbon steel in 3 wt.% NaCl solution. Inserted images showing rust were taken after exposure to the solution.

4.4 AFM characterization of nanocomposites

4.4.1 Morphology characterization of PDMS/hydrophobic silica nanocomposites: Tapping mode AFM

Tapping mode AFM image of a pure PDMS sample is shown in Figure 4.12(a, b). The PDMS matrix appears relatively homogenous as observed in both the height (Figure 4.12a) and phase images (Figure 4.12b). The root mean square (rms) roughness calculated from the height picture is 0.8 ± 0.1 nm. In tapping mode AFM, the phase shift is usually interpreted as being related to the local energy dissipation, such as surface viscoelasticity and tip-sample adhesion.⁸³ We note that with Bruker's digital lock-in controller the drive phase is set to 90° , giving zero phase shift when the tip does not contact the surface.⁸⁴ The average phase reported by the software for our PDMS sample is as low as 0.03° , which suggests high-energy dissipation. From the phase images, we note that the exact value of the phase is not the same all over the surface, which hints a local variation in surface properties. A measure of this heterogeneity can be obtained from the rms variation in the phase angle, which is found to be 1.8° for the image reported in Figure 4.12b.

Tapping mode height and phase contrast images of PDMS with 20 wt.% silica nanoparticles are shown in Figure 4.12(c, d). As expected, the surface of the nanocomposite is significantly more heterogeneous than that of the pure PDMS. The calculated rms roughness in Figure 4.12c is 22 nm, i.e., significantly larger than the value below 1 nm observed for pure PDMS using tapping mode. The phase images of the PDMS-silica nanocomposite (Figure 4.12d) contain three distinguishable regions representing different material constituents: the relatively dark area (smallest phase) is the soft PDMS matrix, the white spots (largest phase) with different

shapes are attributed to the hard silica nanoparticles, and yellow areas (intermediate phase) are the PDMS matrix stiffened by the presence of the particles. The hard silica particles found on the surface give an increase in phase angle (about 30°) compared to that found for the soft PDMS matrix. However, the phase shift on the particles is smaller than that observed for a silicon wafer,⁸⁴ which is due to the response of the soft PDMS matrix in which the nanoparticles are imbedded. The yellow zones seem to be more abundant in regions with high density of silica particles, suggesting an effect of matrix-nanoparticle interactions.

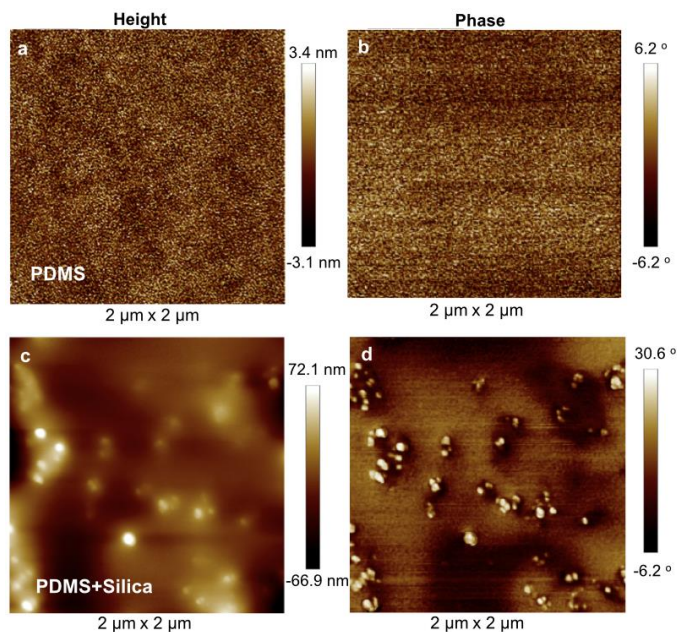


Figure 4.12. Height (a, c) and phase contrast (b, d) images of a pure PDMS and PDMS with 20 wt.% hydrophobic silica nanoparticles spin-coated on silicon wafers recorded by Tapping mode™ AFM. The scan size was $2\ \mu\text{m} \times 2\ \mu\text{m}$.

4.4.2 Nanomechanical characterization of PDMS/hydrophobic silica nanocomposites

4.4.2.1 Intermodulation AFM

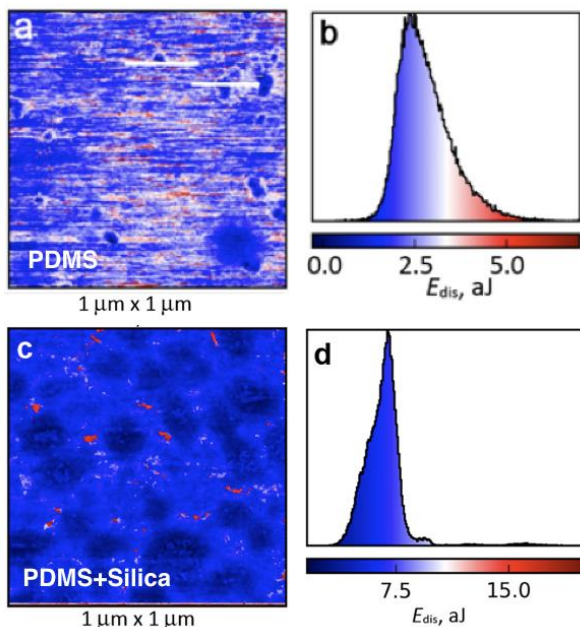


Figure 4.13. Maps of the energy dissipation (E_{dis}) and the corresponding distribution histogram of the nanocomposite with 20 wt.% hydrophobic silica nanoparticles in a PDMS matrix (a, b) and a pure PDMS sample (c, d).

The energy dissipation map and the corresponding dissipation energy distribution histogram for the nanocomposite and pure PDMS are shown in Figure 4.13. The average energy dissipation has significantly decreased after adding the silica nanoparticles in comparison to the energy dissipation measured on pure PDMS, as seen by comparing Figure 4.13b and Figure 4.13d. This correlates qualitatively with previous studies on similar systems using other methods. For example, Fragiadakis et al. studied the glass transition and segmental dynamics in PDMS/silica nanocomposites and found

that the glass transition temperature increased 10 K compared to that of pure PDMS.⁸⁵ For the nanocomposite, the dissipated energy is lower on top of the particles, 0–2 aJ, compared to 2–5 aJ on the matrix. Thus, as expected the energy dissipation is less on the stiffer areas.

4.4.2.2 QI AFM and force mapping on PEMA-PiBMA/hydrophobic silica nanocomposites

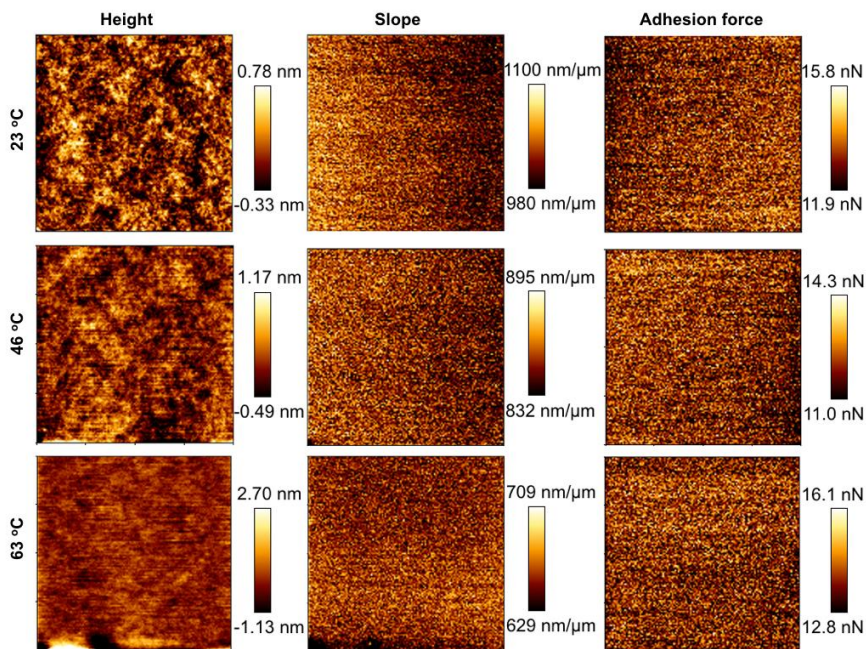


Figure 4.14. QI AFM images of the PEMA-PiBMA polymer matrix without added particles showing height (left column), slope/stiffness (middle column) and adhesion force (right column). The scan size is $2\ \mu\text{m} \times 2\ \mu\text{m}$ for all the images. The images were collected at 23 °C (first row), 46 °C (middle row) and 63 °C (bottom row).

QI images of the PEMA-PiBMA layer in absence of hydrophobic silica nanoparticles are shown in Figure 4.14, including height, slope/stiffness and adhesion force maps over an area of $2\ \mu\text{m} \times 2\ \mu\text{m}$.

The height images demonstrate uniform and homogeneous surface topography throughout the scan area. With increasing temperature, the roughness of the surface increases somewhat, presumably due to uneven thermal expansion. As expected, the surface stiffness, as determined by the slope, is found to decrease with increasing temperature. The adhesion force maps are similar at all investigated temperatures.

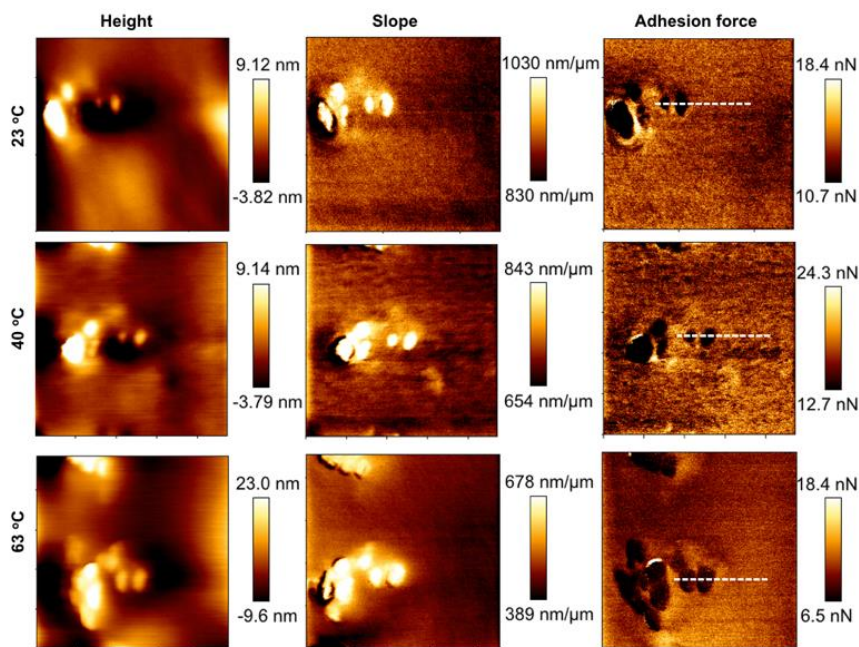


Figure 4.15. QI images of the nanocomposite layer showing height (left column), slope/stiffness (middle column) and adhesion force (right column). The scan size is around 500 nm × 500 nm for all images. From top to bottom the different rows correspond to images recorded at 23, 40 and 63 °C. The scan areas are not exactly the same due to some drift, but the particles marked by the dashed line are observed in all images.

QI images of the PEMA-PiBMA/hydrophobized silica nanocomposite are presented in Figure 4.15 over an area of around 500 nm × 500 nm. Images recorded on heating at 23, 40 and 63 °C are shown. Nanoparticles and their small aggregates can be seen in

the images reported in Figure 4.15. The nanoparticles have higher stiffness and lower adhesion force to the probing tip compared with the polymer matrix. We note that the two individual particles marked with the white dashed line gradually move together with increasing temperature. This is especially clear in the stiffness and adhesion force maps.

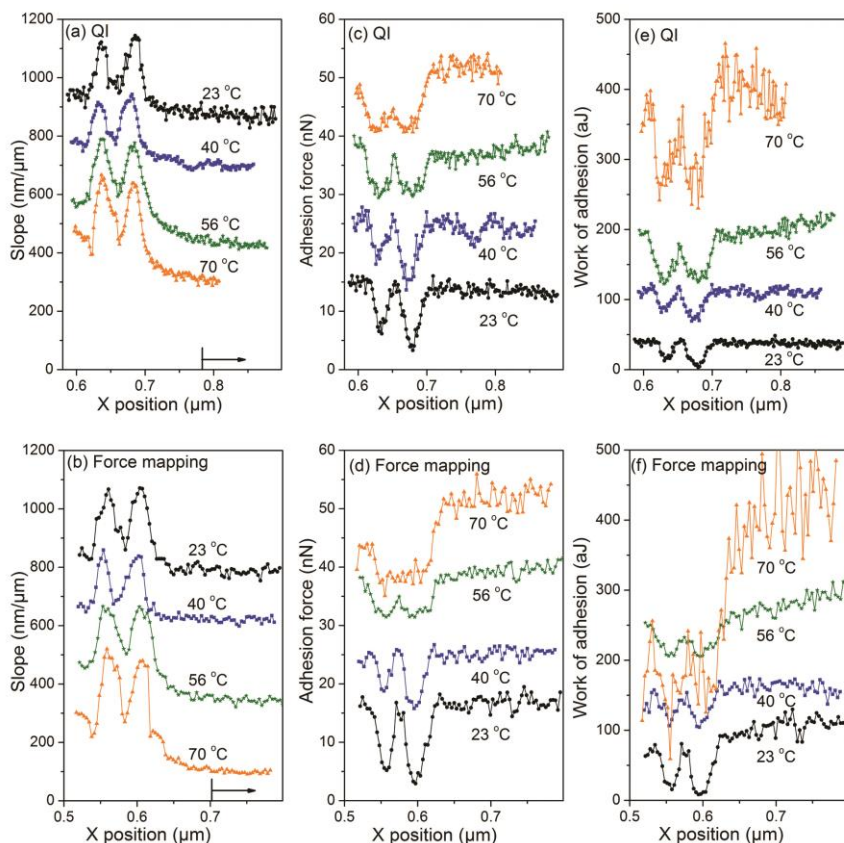


Figure 4.16. Plots of data extracted from QI images and force mapping images for slope/stiffness, adhesion force and work of adhesion (from data taken along the dashed white line marked in Figure 4.15) at different temperatures. Data collected at 23, 40, 56 and 70 °C are shown. (a, b) Slope/stiffness, (c, d) adhesion force and (e, f) work of adhesion. Plots of adhesion force and work of adhesion at 23, 40 and 56 °C overlap each other and different offsets at 40 and 56 °C are used for clarity. There is no offset for the data recorded at 70 °C.

Data extracted for the slope/stiffness, adhesion force and work of adhesion along the white dashed line (shown in Figure 4.15) at 23, 40, 56 and 70 °C are reported in Figure 4.16. The length of the selected line is around 280 nm and the diameter of the rightmost particle is around 40 nm as measured with AFM. Data obtained from QI mode and force mapping mode show the same trend with increasing temperature for the evaluated mechanical properties. The two nanoparticles can be clearly identified in the property maps of Figure 4.16 as they are distinguished by higher stiffness, lower adhesion force and work of adhesion compared with the polymer matrix. The temperature affects the surface interphase region and the surface of the polymer matrix differently, although both regions show a decrease in stiffness and increase in the work of adhesion with increasing temperature. Further, we note that the difference in mechanical properties recorded on particles and on the polymer matrix also becomes larger with increasing temperature. In particular, the work of adhesion recorded at 70 °C (Figure 4.16e and 4.16f) is very different over the nanoparticles and the polymer matrix.

4.4.3 Nanomechanical properties of the interphase found in the PEMA-PiBMA/hydrophobized silica nanocomposite

From Figure 4.16 we also find that the stiffness of the interphase is higher than that of the polymer matrix, but lower than that on top of the nanoparticles. The results indicate that the interphase region exhibits a gradient in stiffness, being most stiff close to the particle and smoothly approaching the stiffness of the matrix as the distance from the particle is increased. This is due to a decreasing confinement effect on the polymer further away from the nanoparticle surface. The confinement is due to the attractive interaction between the hydrophobized silica nanoparticles and the

polymer matrix as well as the spatial hindrance by the presence of the nanoparticles, leading to reduction in the polymer chain mobility.^{86,87}

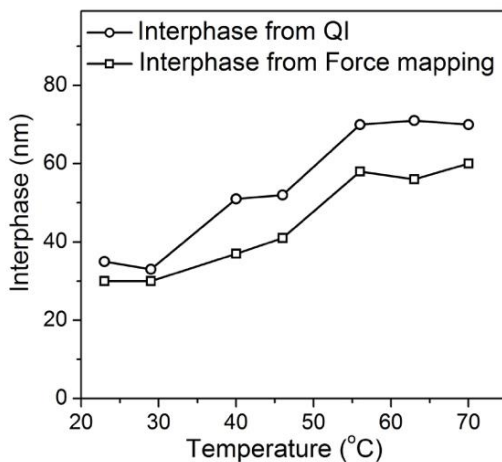


Figure 4.17. The temperature dependence of the thickness of the interphase region determined from QI and force mapping mode, respectively.

The temperature dependence of the thickness of the interphase region determined from QI and force mapping is reported in Figure 4.17. It is found to be 30–35 nm next to a 40-nm-diameter particle at 23 °C. With increasing temperature, the thickness of this region first increases and then remains almost constant from 56 °C to 70 °C. The same trends can be observed in both QI and force mapping modes. This trend contrasts to the findings of Deng et al. and Wang et al., employing dynamics simulations, that suggest the interphase thickness should decrease with increasing temperature.^{88,89} This difference could possibly be due to the different nature of the nanocomposites and the different definitions of the interphase region used in this thesis and their simulations. First, the studies of Deng et al. and Wang et al. consider covalent highly cross-linked rubber or epoxy, and the chain mobility in the matrix is therefore

significantly restricted.^{88,89} In contrast, in this thesis a matrix consisting of linear polymers is employed, and the chains in the polymer matrix are more mobile than in the interphase region due to confinement effects of the nanoparticles. Second, in this thesis the interphase is defined by different mechanical properties compared to the bulk polymer matrix, and thus the thickness determined is influenced by the sensitivity of the technique used and the contrast between interphase and matrix properties. This contrast is increasing with increasing temperature, leading to a larger interphase thickness as judged from the surface mechanical properties evaluated by AFM methods. An artificial increase in interphase thickness could also occur if the tip-surface contact area increases as the polymer becomes softer with increasing temperature.

At 56 °C, the surface interphase region reaches a thickness of 55–70 nm. Despite an inherent uncertainty in the interphase thickness, these results support the existence of an interphase region with different properties from that of the matrix, as suggested in several previous works.^{57,90-93} Moreover, the volume of the interphase in a nanocomposite is huge and a reinforcing network could be formed even at a very low concentration. This is why nanomaterials often have better properties than their counterpart bulk material or composite materials with micro-sized particles.

Chapter 5 Conclusions and impact

In this thesis work, novel electrochemical sensors to simultaneously detect Cd^{2+} and Pb^{2+} ions using DPASV have been developed. Further, for corrosion protection with self-healing functionality, an active alkyd-polyaniline composite coating was prepared. It was also investigated why low loading levels of nanoparticles can reinforce performance in nanocomposites. The main conclusions are summarized as follows.

1. A G-MWCNTs nanocomposite was successfully fabricated via an environmentally benign method and its potential application in the simultaneous detection of Cd^{2+} and Pb^{2+} ions was demonstrated. The G-MWCNTs modified GCE electrode exhibited high sensitivity for the detection of trace amounts of Pb^{2+} and Cd^{2+} ions, with the lowest detection concentration of $0.5 \mu\text{g L}^{-1}$ for Cd^{2+} and $0.5 \mu\text{g L}^{-1}$ for Pb^{2+} . The greatly enhanced detection sensitivity of the nanocomposite was due to the synergistic effect between the MWCNTs and graphene components in improving preconcentration efficiency of metal ions and accelerating electron transfer rates at the G-MWCNTs/electrolyte interface.

2. One dimensional phytic acid doped PANI nanocomposite was successfully synthesized by a facile method, which can be used as an ideal platform to simultaneously detect Cd^{2+} and Pb^{2+} ions using DPASV, with the detection limits ($S/N = 3$) of $0.02 \mu\text{g L}^{-1}$ and $0.05 \mu\text{g L}^{-1}$, respectively. Compared with the H_2SO_4 doped PANI nanofibers modified electrode, the enhanced detection sensitivity was assigned to the introduction of $-\text{PO}_3\text{H}_2$ groups, which was advantageous to the deposition of heavy metal ions, and the enhanced conductivity that is beneficial to the charge transfer reactions of metal ions. Therefore, the synergistic contribution of PANI nanofibers and phytic acid made the new electrode material a capable candidate for the detection of trace levels of heavy metal ions. The two

developments described under point 1 and 2 have the potential to allow accurate and rapid assessment of metal ion concentrations in water, which can have positive impact of both human health and the environment.

3. An active alkyd composite coating with 1 wt.% PANI was used for long-term anticorrosion protection. The PANI used in this thesis was doped with p-toluene sulfonic acid, which was employed to increase the conductivity of PANI, and only 1 wt.% of as-prepared PANI nanoparticles were found to offer an effective corrosion protection. The OCP vs. time of exposure tests in 3 wt.% NaCl solution results confirmed the improved protection properties, which was due to the self-healing effect of the PANI, i.e., the steel surface with defects became oxidized while the covered PANI was reduced. This is important since the most efficient corrosion protection systems used today contain substance (e.g. Cr(VI)) that are dangerous to human health and the environment. Thus, my work suggests ways forward for achieving efficient corrosion protection using environmentally benign approaches.

4. Several different AFM modes were used to characterize silica nanoparticles based nanocomposite with focus on the interphase between hydrophobic silica and the polymer matrix. The results demonstrated that the interphase for a 40-nm-sized silica particle could extend to 55–70 nm in the poly(ethyl methacrylate) (PEMA) and poly(isobutyl methacrylate) (PiBMA) polymer matrix, and the interphase exhibited a gradient distribution in surface nanomechanical properties. To understand how properties of nanocomposites are affected by particle-polymer interactions, as witnessed by the interphase properties, is of great importance for development of nanocomposites with tailored mechanical and functional properties. My work has demonstrated that AFM methods have great potential for evolving the understanding in this important area.

Chapter 6 Future work

Research on development and application of nanomaterials and nanocomposites is currently one of the most active areas in electrochemical sensor science. Traditional materials based techniques are expected to be replaced by nanomaterials in the near future. This development requires advances in mainly two areas: i) the development of novel nanomaterials and ii) the engineering design for practical applications. Specifically, they are as follows.

i) Despite of the two works already completed in this thesis and various previously reported works by others, there is still plenty of room for the improvement of graphene- or polyaniline-based nanocomposites. One idea could be to synthesize phytic acid doped rGO hybrid material and employ it as a detection platform for heavy metal ions, since rGO possesses good conductivity, high surface area and versatile reaction sites while phytic acids chelating groups increase the preconcentration efficiency for metal ions. Hopefully, phytic acid could also inhibit the aggregation of rGO. Another idea could be to prepare ternary complexes, e.g., phytic acid/polyaniline/graphene composites. The three components are expected to provide synergistic effects for detecting heavy metal ions. Further, there is still demand for the design of selective electrodes for specific metal ions. In addition, it would be of great interesting to assess the potential applications for the above-mentioned nanocomposites in corrosion protection for metals, e.g., carbon steel.

ii) Although it is always claimed that an easy and simple method was proposed to prepare some kind of modified electrode, this is just the case referred to under laboratory analysis. Once realizing commercialization, end-customers with different background is likely to complain about the complicated procedures to prepare the modified electrodes. Therefore, the production method is of vital

importance. Screen-printed electrodes (SPE) are simple and cheap, and allow large-scale production with good reproducibility. Future work involving SPE combined with graphene- or polyaniline-based nanocomposites will be assured to enable fast, on-site or in-situ analysis of heavy metal ions.

For the characterization of nanocomposites, especially for the study of interphase properties, future work to clarify the detailed nature of the interphase employing also other techniques that provide complementary information, e.g., nuclear magnetic resonance spectroscopy, is required. In addition, the combination of theoretical modeling based on molecular dynamics method and experimental measurements on the studies of mechanical properties of the nanocomposites is also highly desired.

Acknowledgments

I would like to express my sincere appreciation to a number of people who have made this thesis possible.

First, I would like to acknowledge my main supervisor, Prof. Per Claesson, for giving me the opportunity to study at KTH. He is really a great supervisor and mentor, and I have learnt a lot from him during his lectures, the regular seminars and our meetings.

I would like to express my greatest gratitude to my co-supervisor, Prof. Jinshan Pan for offering me the opportunity to join in the Division of Surface and Corrosion Science.

I would like to thank my supervisor in China, Prof. Houyi Ma, for admitting me as a PhD student in Shandong University and allowing me to continue my study at KTH. He is a respectable supervisor, and it is really a great treasure to work with him.

I would like to thank my co-authors, Dr. Illia Dobryden, Per-Anders Thorén, Dr. Lina Ejenstam, Dr. Matthew Fielden, Prof. David Haviland, Niklas Ihrner, Prof. Mats Johansson, Dr. Jing Li, Dr. Ting Chen and Dr. Wencai Zhu. It has been a great pleasure to work with all of them. Special thanks to Dr. Matthew Fielden for training me to use AFM. Special thanks to Dr. Illia Dobryden for his help in script implementing in the Intermodulation AFM data analysis.

Many thanks to Qiliang Fu in the division of Biocomposites & Wallenberg Wood Science Center for the fruitful discussions and measurements. Thanks to Assoc. Prof. Eva Blomberg for creating such a good atmosphere in our division.

Thanks to Dr. Fan Zhang, Junxue An, Litao Yin, Tingru Chang, Chengdong Chen, Dr. Xian Zhang, Dr. Xiaoyan Liu, Dr. Min Wang, Prof. Christofer Leygraf, Prof. Inger Odnevall Wallinder, Assoc. Prof. Eric Tyrode, Assoc. Prof. Andra Dédinaité, Prof. Mark Rutland, Assoc. Prof. Magnus Johnson, Dr. Gunilla Herting, Dr. Deborah Wakeham, Dr. Rasmus Bodvik, Dr. Jonas Hedberg, Dr. Zahra Besharat, Krishnan

Hariramabadran Anantha, Sulena Pradhan, Akanksha Raj, Sara Skoglund, Adrien Sthoer, Dr. Neda Mazinianian, Marie Långberg, Gen Li, Min Liu and many other current and former colleagues in the division for their help.

Thanks to many other benign friends in Sweden and China for their encouragement and accompany. Special thanks to Dr. Xiang Sheng and his wife Hongyu Xie for their consideration in daily life, especially when my family was not with me in Sweden.

Financial support from the China Scholarship Council is acknowledged.

I would like to thank my parents, my sister and brother and their families for their support and understanding.

Finally, I would like to thank my husband Guangping Zhang for all his love and patience. I feel lucky to have him in my life.

References

- (1) D.R. Thévenot, K. Toth, R.A. Durst, G.S. Wilson, Electrochemical biosensors: recommended definitions and classification, *Biosensors and Bioelectronics*, 16 (2001) 121-131.
- (2) J. Molina, F. Cases, L. Moretto, Graphene-based materials for the electrochemical determination of hazardous ions, *Analytica Chimica Acta*, 946 (2016) 9-39.
- (3) X.-J. Huang, Y.-K. Choi, Chemical sensors based on nanostructured materials, *Sensors and Actuators B: Chemical*, 122 (2007) 659-671.
- (4) E. Fischer, C.M. van den Berg, Anodic stripping voltammetry of lead and cadmium using a mercury film electrode and thiocyanate, *Analytica Chimica Acta*, 385 (1999) 273-280.
- (5) K. Wu, S. Hu, J. Fei, W. Bai, Mercury-free simultaneous determination of cadmium and lead at a glassy carbon electrode modified with multi-wall carbon nanotubes, *Analytica Chimica Acta*, 489 (2003) 215-221.
- (6) Y.S. Kim, H.S. Jung, T. Matsuura, H.Y. Lee, T. Kawai, M.B. Gu, Electrochemical detection of 17 β -estradiol using DNA aptamer immobilized gold electrode chip, *Biosensors and Bioelectronics*, 22 (2007) 2525-2531.
- (7) J. Wang, Stripping analysis at bismuth electrodes: a review, *Electroanalysis*, 17 (2005) 1341-1346.
- (8) W.W. Zhu, N.B. Li, H.Q. Luo, Simultaneous determination of chromium (III) and cadmium (II) by differential pulse anodic stripping voltammetry on a stannum film electrode, *Talanta*, 72 (2007) 1733-1737.
- (9) G. March, T.D. Nguyen, B. Piro, Modified electrodes used for electrochemical detection of metal ions in environmental analysis, *Biosensors*, 5 (2015) 241-275.
- (10) Z. Wang, E. Liu, X. Zhao, Glassy carbon electrode modified by conductive polyaniline coating for determination of trace lead and cadmium ions in acetate buffer solution, *Thin Solid Films*, 519 (2011) 5285-5289.

- (11) J. Morton, N. Havens, A. Mugweru, A.K. Wanekaya, Detection of trace heavy metal ions using carbon nanotube-modified electrodes, *Electroanalysis*, 21 (2009) 1597-1603.
- (12) J. Li, S. Guo, Y. Zhai, E. Wang, Nafion-graphene nanocomposite film as enhanced sensing platform for ultrasensitive determination of cadmium, *Electrochemistry Communications*, 11 (2009) 1085-1088.
- (13) M.F. Philips, A.I. Gopalan, K.-P. Lee, Development of a novel cyano group containing electrochemically deposited polymer film for ultrasensitive simultaneous detection of trace level cadmium and lead, *Journal of Hazardous Materials*, 237 (2012) 46-54.
- (14) L. Chen, Z. Su, X. He, Y. Liu, C. Qin, Y. Zhou, Z. Li, L. Wang, Q. Xie, S. Yao, Square wave anodic stripping voltammetric determination of Cd and Pb ions at a Bi/Nafion/thiolated polyaniline/glassy carbon electrode, *Electrochemistry Communications*, 15 (2012) 34-37.
- (15) N. Ruecha, N. Rodthongkum, D.M. Cate, J. Volckens, O. Chailapakul, C.S. Henry, Sensitive electrochemical sensor using a graphene-polyaniline nanocomposite for simultaneous detection of Zn (II), Cd (II), and Pb (II), *Analytica Chimica Acta*, 874 (2015) 40-48.
- (16) N. Promphet, P. Rattanarat, R. Rangkupan, O. Chailapakul, N. Rodthongkum, An electrochemical sensor based on graphene/polyaniline/polystyrene nanoporous fibers modified electrode for simultaneous determination of lead and cadmium, *Sensors and Actuators B: Chemical*, 207 (2015) 526-534.
- (17) J. Kong, A.M. Cassell, H. Dai, Chemical vapor deposition of methane for single-walled carbon nanotubes, *Chemical Physics Letters*, 292 (1998) 567-574.
- (18) J.-F. Colomer, C. Stephan, S. Lefrant, G. Van Tendeloo, I. Willems, Z. Konya, A. Fonseca, C. Laurent, J.B. Nagy, Large-scale synthesis of single-wall carbon nanotubes by catalytic chemical vapor deposition (CCVD) method, *Chemical Physics Letters*, 317 (2000) 83-89.

- (19) W.S. Hummers Jr, R.E. Offeman, Preparation of graphitic oxide, *Journal of the American Chemical Society*, 80 (1958) 1339-1339.
- (20) D.C. Marcano, D.V. Kosynkin, J.M. Berlin, A. Sinitskii, Z. Sun, A. Slesarev, L.B. Alemany, W. Lu, J.M. Tour, Improved synthesis of graphene oxide, *ACS Nano*, 4 (2010) 4806-4814.
- (21) C.K. Chiang, C. Fincher Jr, Y.W. Park, A.J. Heeger, H. Shirakawa, E.J. Louis, S.C. Gau, A.G. MacDiarmid, Electrical conductivity in doped polyacetylene, *Physical Review Letters*, 39 (1977) 1098.
- (22) S. Virji, J. Huang, R.B. Kaner, B.H. Weiller, Polyaniline nanofiber gas sensors: examination of response mechanisms, *Nano Letters*, 4 (2004) 491-496.
- (23) D. Li, J. Huang, R.B. Kaner, Polyaniline nanofibers: a unique polymer nanostructure for versatile applications, *Accounts of Chemical Research*, 42 (2008) 135-145.
- (24) C. Dhand, M. Das, M. Datta, B. Malhotra, Recent advances in polyaniline based biosensors, *Biosensors and Bioelectronics*, 26 (2011) 2811-2821.
- (25) Z. Su, Y. Liu, Y. Zhang, Q. Xie, L. Chen, Y. Huang, Y. Fu, Y. Meng, X. Li, M. Ma, Thiol-ene chemistry guided preparation of thiolated polymeric nanocomposite for anodic stripping voltammetric analysis of Cd^{2+} and Pb^{2+} , *Analyst*, 138 (2013) 1180-1186.
- (26) A. Terbouche, C. Ait-Ramdane-Terbouche, S. Djebbar, O. Benali-Baitich, D. Hauchard, Effectiveness study of sensor based on modified cavity microelectrode by Algerian humic acid-polyaniline composites using square wave voltammetry, *Sensors and Actuators B: Chemical*, 169 (2012) 297-304.
- (27) Y. Wang, X. Ma, Y. Wen, Y. Zheng, G. Duan, Z. Zhang, H. Yang, Phytic acid-based layer-by-layer assembly for fabrication of mesoporous gold film and its biosensor application, *Journal of the Electrochemical Society*, 157 (2010) K5-K9.
- (28) H. Persson, M. Türk, M. Nyman, A.-S. Sandberg, Binding of Cu^{2+} , Zn^{2+} , and Cd^{2+} to inositol tri-, tetra-, penta-, and hexaphosphates, *Journal of Agricultural and Food Chemistry*, 46 (1998) 3194-3200.

- (29) C. Hao, R.-H. Yin, Z.-Y. Wan, Q.-J. Xu, G.-D. Zhou, Electrochemical and photoelectrochemical study of the self-assembled monolayer phytic acid on cupronickel B30, *Corrosion Science*, 50 (2008) 3527-3533.
- (30) L. Ejenstam, A. Swerin, J. Pan, P.M. Claesson, Corrosion protection by hydrophobic silica particle-polydimethylsiloxane composite coatings, *Corrosion Science*, 99 (2015) 89-97.
- (31) J. Godt, F. Scheidig, C. Grosse-Siestrup, V. Esche, P. Brandenburg, A. Reich, D.A. Groneberg, The toxicity of cadmium and resulting hazards for human health, *Journal of Occupational Medicine and Toxicology*, 1 (2006) 1.
- (32) A.K. Meena, G. Mishra, P. Rai, C. Rajagopal, P. Nagar, Removal of heavy metal ions from aqueous solutions using carbon aerogel as an adsorbent, *Journal of Hazardous Materials*, 122 (2005) 161-170.
- (33) J. Duruibe, M. Ogwuegbu, J. Ekwurugwu, Heavy metal pollution and human biotoxic effects, *International Journal of Physical Sciences*, 2 (2007) 112-118.
- (34) G. Zhu, C.-y. Zhang, Functional nucleic acid-based sensors for heavy metal ion assays, *Analyst*, 139 (2014) 6326-6342.
- (35) I. Rutyna, M. Korolczuk, Determination of lead and cadmium by anodic stripping voltammetry at bismuth film electrodes following double deposition and stripping steps, *Sensors and Actuators B: Chemical*, 204 (2014) 136-141.
- (36) W. Yantasee, Y. Lin, G.E. Fryxell, B.J. Busche, Simultaneous detection of cadmium, copper, and lead using a carbon paste electrode modified with carbamoylphosphonic acid self-assembled monolayer on mesoporous silica (SAMMS), *Analytica Chimica Acta*, 502 (2004) 207-212.
- (37) G. Zhu, Y. Li, C.-y. Zhang, Simultaneous detection of mercury (II) and silver (I) ions with picomolar sensitivity, *Chemical Communications*, 50 (2014) 572-574.
- (38) M.L. Zheludkevich, D.G. Shchukin, K.A. Yasakau, H. Möhwald, M.G. Ferreira, Anticorrosion coatings with self-healing effect based on nanocontainers impregnated with corrosion inhibitor, *Chemistry of Materials*, 19 (2007) 402-411.

- (39) S. Radhakrishnan, C. Siju, D. Mahanta, S. Patil, G. Madras, Conducting polyaniline–nano-TiO₂ composites for smart corrosion resistant coatings, *Electrochimica Acta*, 54 (2009) 1249-1254.
- (40) M. Moniruzzaman, K.I. Winey, Polymer nanocomposites containing carbon nanotubes, *Macromolecules*, 39 (2006) 5194-5205.
- (41) J.R. Potts, D.R. Dreyer, C.W. Bielawski, R.S. Ruoff, Graphene-based polymer nanocomposites, *Polymer*, 52 (2011) 5-25.
- (42) J. Fröhlich, W. Niedermeier, H.-D. Luginsland, The effect of filler–filler and filler–elastomer interaction on rubber reinforcement, *Composites Part A: Applied Science and Manufacturing*, 36 (2005) 449-460.
- (43) F. Mammeri, E. Le Bourhis, L. Rozes, C. Sanchez, Mechanical properties of hybrid organic–inorganic materials, *Journal of Materials Chemistry*, 15 (2005) 3787-3811.
- (44) L. Dewimille, B. Bresson, L. Bokobza, Synthesis, structure and morphology of poly (dimethylsiloxane) networks filled with in situ generated silica particles, *Polymer*, 46 (2005) 4135-4143.
- (45) H. Hu, L. Onyebueke, A. Abatan, Characterizing and modeling mechanical properties of nanocomposites-review and evaluation, *Journal of Minerals and Materials Characterization and Engineering*, 9 (2010) 275.
- (46) H. Liu, L.C. Brinson, Reinforcing efficiency of nanoparticles: a simple comparison for polymer nanocomposites, *Composites Science and Technology*, 68 (2008) 1502-1512.
- (47) R.A. Vaia, H.D. Wagner, Framework for nanocomposites, *Materials Today*, 7 (2004) 32-37.
- (48) H.D. Wagner, R.A. Vaia, Nanocomposites: issues at the interface, *Materials Today*, 7 (2004) 38-42.
- (49) Y. Zare, Development of Halpin-Tsai model for polymer nanocomposites assuming interphase properties and nanofiller size, *Polymer Testing*, 51 (2016) 69-73.
- (50) S. Kaufman, W. Slichter, D. Davis, Nuclear magnetic resonance study of rubber–carbon black interactions, *Journal of Polymer Science Part A - 2: Polymer Physics*, 9 (1971) 829-839.

- (51) S. Marceau, P. Dubois, R. Fulchiron, P. Cassagnau, Viscoelasticity of Brownian carbon nanotubes in PDMS semidilute regime, *Macromolecules*, 42 (2009) 1433-1438.
- (52) F. Gojny, M. Wichmann, U. Köpke, B. Fiedler, K. Schulte, Carbon nanotube-reinforced epoxy-composites: enhanced stiffness and fracture toughness at low nanotube content, *Composites Science and Technology*, 64 (2004) 2363-2371.
- (53) S.K. Kumar, N. Jouault, B. Benicewicz, T. Neely, Nanocomposites with polymer grafted nanoparticles, *Macromolecules*, 46 (2013) 3199-3214.
- (54) D. Paul, L. Robeson, Polymer nanotechnology: nanocomposites, *Polymer*, 49 (2008) 3187-3204.
- (55) D.S. Simmons, An Emerging Unified View of Dynamic Interphases in Polymers, *Macromolecular Chemistry and Physics*, 217 (2016) 137-148.
- (56) Y. Gu, M. Li, J. Wang, Z. Zhang, Characterization of the interphase in carbon fiber/polymer composites using a nanoscale dynamic mechanical imaging technique, *Carbon*, 48 (2010) 3229-3235.
- (57) C.L. Wu, M.Q. Zhang, M.Z. Rong, K. Friedrich, Tensile performance improvement of low nanoparticles filled-polypropylene composites, *Composites Science and Technology*, 62 (2002) 1327-1340.
- (58) D. Li, M.B. Müller, S. Gilje, R.B. Kaner, G.G. Wallace, Processable aqueous dispersions of graphene nanosheets, *Nature Nanotechnology*, 3 (2008) 101-105.
- (59) W. Li, M. Wan, Porous polyaniline films with high conductivity, *Synthetic Metals*, 92 (1998) 121-126.
- (60) G. Zhang, F. Yang, Direct electrochemistry and electrocatalysis of anthraquinone-monosulfonate/polyaniline hybrid film synthesized by a novel electrochemical doping-dedoping-redoping method on pre-activated spectroscopically pure graphite surface, *Physical Chemistry Chemical Physics*, 13 (2011) 3291-3302.

- (61) W. Li, M. Wan, Stability of polyaniline synthesized by a doping–dedoping–redoping method, *Journal of Applied Polymer Science*, 71 (1999) 615-621.
- (62) J. Huang, R.B. Kaner, Nanofiber formation in the chemical polymerization of aniline: a mechanistic study, *Angewandte Chemie*, 116 (2004) 5941-5945.
- (63) C. Liu, Recent developments in polymer MEMS, *Advanced Materials*, 19 (2007) 3783-3790.
- (64) F. Surivet, T.M. Lam, J.P. Pascault, C. Mai, Organic-inorganic hybrid materials. 2. Compared structures of polydimethylsiloxane and hydrogenated polybutadiene based ceramers, *Macromolecules*, 25 (1992) 5742-5751.
- (65) Struers safety data sheet. http://www.struers.com/Content/Documents/SDS/VIAFIX_LIQUID/VIAFIX_LIQUID_GB_EN_M0145_13.0_11-02-2016.pdf (accessed Feb 11, 2016).
- (66) Struers safety data sheet. http://www.struers.com/Content/Documents/SDS/VIAFIX_POWDER/VIAFIX_POWDER_GB_EN_M0149_12.0_12-02-2016.pdf (accessed Feb 12, 2016).
- (67) L. Ejenstam, A. Swerin, P.M. Claesson, Toward Superhydrophobic Polydimethylsiloxane–Silica Particle Coatings, *Journal of Dispersion Science and Technology*, 37 (2016) 1375-1383.
- (68) S.R. Sandler, W. Karo, *Polymer Syntheses: Volume I*, Academic Press, 1992.
- (69) C. Finch, *Encyclopaedia of polymer science and engineering*, volume 1, a to amorphous polymers, *British Polymer Journal*, 17 (1985) 321-321.
- (70) D.B. Hall, A. Dhinojwala, J.M. Torkelson, Translation-rotation paradox for diffusion in glass-forming polymers: The role of the temperature dependence of the relaxation time distribution, *Physical Review Letters*, 79 (1997) 103.
- (71) M. Neo, S. Goh, Miscibility of poly (2-bromoethyl methacrylate) with various polymethacrylates, *Macromolecules*, 24 (1991) 2564-2565.

- (72) D.S. Knight, W.B. White, Characterization of diamond films by Raman spectroscopy, *Journal of Materials Research*, 4 (1989) 385-393.
- (73) D. Platz, D. Forchheimer, E.A. Tholén, D.B. Haviland, Interaction imaging with amplitude-dependence force spectroscopy, *Nature Communications*, 4 (2013) 1360.
- (74) D. Forchheimer, R. Forchheimer, D.B. Haviland, Improving image contrast and material discrimination with nonlinear response in bimodal atomic force microscopy, *Nature Communications*, 6 (2015) 6270.
- (75) D. Platz, D. Forchheimer, E.A. Tholén, D.B. Haviland, The role of nonlinear dynamics in quantitative atomic force microscopy, *Nanotechnology*, 23 (2012) 265705.
- (76) S.S. Borysov, D. Platz, A.S. de Wijn, D. Forchheimer, E.A. Tolén, A.V. Balatsky, D.B. Haviland, Reconstruction of tip-surface interactions with multimodal intermodulation atomic force microscopy, *Physical Review B*, 88 (2013) 115405.
- (77) D.B. Haviland, C.A. van Eysden, D. Forchheimer, D. Platz, H.G. Kassa, P. Leclère, Probing viscoelastic response of soft material surfaces at the nanoscale, *Soft Matter*, 12 (2016) 619-624.
- (78) M. Higgins, R. Proksch, J.E. Sader, M. Polcik, S. Mc Endoo, J. Cleveland, S. Jarvis, Noninvasive determination of optical lever sensitivity in atomic force microscopy, *Review of Scientific Instruments*, 77 (2006) 013701.
- (79) J.E. Sader, Frequency response of cantilever beams immersed in viscous fluids with applications to the atomic force microscope, *Journal of Applied Physics*, 84 (1998) 64-76.
- (80) L. Chopinet, C. Formosa, M. Rols, R. Duval, E. Dague, Imaging living cells surface and quantifying its properties at high resolution using AFM in QI™ mode, *Micron*, 48 (2013) 26-33.
- (81) J.E. Sader, J.W. Chon, P. Mulvaney, Calibration of rectangular atomic force microscope cantilevers, *Review of Scientific Instruments*, 70 (1999) 3967-3969.
- (82) C.P. Green, H. Lioe, J.P. Cleveland, R. Proksch, P. Mulvaney, J.E. Sader, Normal and torsional spring constants of atomic force

- microscope cantilevers, *Review of Scientific Instruments*, 75 (2004) 1988-1996.
- (83) J. Cleveland, B. Anczykowski, A. Schmid, V. Elings, Energy dissipation in tapping-mode atomic force microscopy, *Applied Physics Letters*, 72 (1998) 2613-2615.
- (84) S. Magonov, V. Elings, M.-H. Whangbo, Phase imaging and stiffness in tapping-mode atomic force microscopy, *Surface Science*, 375 (1997) L385-L391.
- (85) D. Fragiadakis, P. Pissis, Glass transition and segmental dynamics in poly (dimethylsiloxane)/silica nanocomposites studied by various techniques, *Journal of Non-Crystalline Solids*, 353 (2007) 4344-4352.
- (86) G.P. Baeza, C. Dessi, S. Costanzo, D. Zhao, S. Gong, A. Alegria, R.H. Colby, M. Rubinstein, D. Vlassopoulos, S.K. Kumar, Network dynamics in nanofilled polymers, *Nature Communications*, 7 (2016) 11368.
- (87) A. Bansal, H. Yang, C. Li, K. Cho, B.C. Benicewicz, S.K. Kumar, L.S. Schadler, Quantitative equivalence between polymer nanocomposites and thin polymer films, *Nature Materials*, 4 (2005) 693-698.
- (88) F. Deng, K.J. Van Vliet, Prediction of elastic properties for polymer-particle nanocomposites exhibiting an interphase, *Nanotechnology*, 22 (2011) 165703.
- (89) Z. Wang, Q. Lv, S. Chen, C. Li, S. Sun, S. Hu, Effect of Interfacial Bonding on Interphase Properties in SiO₂/Epoxy Nanocomposite: A Molecular Dynamics Simulation Study, *ACS Applied Materials & Interfaces*, 8 (2016) 7499-7508.
- (90) K.I. Winey, R.A. Vaia, Polymer nanocomposites, *MRS bulletin*, 32 (2007) 314-322.
- (91) J. Li, H. Huang, M. Fielden, J. Pan, L. Ecco, C. Schellbach, G. Delmas, P.M. Claesson, Towards the mechanism of electrochemical activity and self-healing of 1 wt% PTSA doped polyaniline in alkyd composite polymer coating: combined AFM-based studies, *RSC Advances*, 6 (2016) 19111-19127.

- (92) J. Sandler, J. Kirk, I. Kinloch, M. Shaffer, A. Windle, Ultra-low electrical percolation threshold in carbon-nanotube-epoxy composites, *Polymer*, 44 (2003) 5893-5899.
- (93) R.H. Baughman, A.A. Zakhidov, W.A. de Heer, Carbon nanotubes--the route toward applications, *Science*, 297 (2002) 787-792.